

IMMUNOBIOLOGY AND IMMUNOTHERAPY

PD-1/PD-L1 immune checkpoint and p53 loss facilitate tumor progression in activated B-cell diffuse large B-cell lymphomas

Marién Pascual,¹ María Mena-Varas,¹ Eloy Francisco Robles,¹ María-José García-Barchino,¹ Carlos Panizo,² Sandra Hervas-Stubbs,³ Diego Alignani,⁴ Ainara Sagardoy,¹ Jose Ignacio Martínez-Ferrandis,¹ Karen L. Bunting,^{5,6} Stephen Meier,⁷ Xavier Sagaert,⁸ Davide Bagnara,^{9,10} Elizabeth Guruceaga,¹¹ Oscar Blanco,¹² Jon Celay,¹ Alvaro Martínez-Baztan,¹ Noelia Casares,³ Juan José Lasarte,³ Thomas MacCarthy,⁷ Ari Melnick,⁶ Jose Angel Martínez-Climent,¹ and Sergio Roa¹

¹Hemato-Oncology Program, Centro de Investigación Médica Aplicada, Instituto de Investigación Sanitaria de Navarra, CIBERONC, University of Navarra, Pamplona, Spain; ²Department of Hematology, Clínica Universidad de Navarra, Instituto de Investigación Sanitaria de Navarra, University of Navarra, Pamplona, Spain; ³Immunology and Immunotherapy Program, Centro de Investigación Médica Aplicada, Instituto de Investigación Sanitaria de Navarra, University of Navarra, Pamplona, Spain; ⁴Cytometry Unit, Centro de Investigación Médica Aplicada, Instituto de Investigación Sanitaria de Navarra, CIBERONC, University of Navarra, Pamplona, Spain; ⁵New York Genome Center, New York, NY; ⁶Department of Medicine/Hematology-Oncology, Weill Cornell Medical College, New York, NY; ⁷Department of Applied Mathematics and Statistics, Stony Brook University, Stony Brook, NY; ⁸Centre for Translation Cell and Tissue Research, KU Leuven, Leuven, Belgium; ⁹Karlsruhe Center for Oncology Research, Feinstein Institute for Medical Research, Northwell Health, Manhasset, NY; ¹⁰Department of Experimental Medicine, University of Genoa, Genoa, Italy; ¹¹Bioinformatics Platform, Centro de Investigación Médica Aplicada, Instituto de Investigación Sanitaria de Navarra, ProteoRed-ISCIII, University of Navarra, Pamplona, Spain; and ¹²Department of Pathology, University of Salamanca, Salamanca, Spain

KEY POINTS

- Constitutive NF-κB activation and blocked terminal differentiation trigger p53 signaling and antitumor immune escape mechanisms in ABC-DLBCL.
- Simultaneous PD-1 blockade improves long-term efficacy of anti-CD20 immunotherapy in a multilesion preclinical mouse model of ABC-DLBCL.

Refractory or relapsed diffuse large B-cell lymphoma (DLBCL) often associates with the activated B-cell-like (ABC) subtype and genetic alterations that drive constitutive NF-κB activation and impair B-cell terminal differentiation. Here, we show that DNA damage response by p53 is a central mechanism suppressing the pathogenic cooperation of IKK2α-enforced canonical NF-κB and impaired differentiation resulting from Blimp1 loss in ABC-DLBCL lymphomagenesis. We provide evidences that the interplay between these genetic alterations and the tumor microenvironment select for additional molecular addictions that promote lymphoma progression, including aberrant coexpression of FOXP1 and the B-cell mutagenic enzyme activation-induced deaminase, and immune evasion through major histocompatibility complex class II downregulation, PD-L1 upregulation, and T-cell exhaustion. Consistently, PD-1 blockade cooperated with anti-CD20-mediated B-cell cytotoxicity, promoting extended T-cell reactivation and antitumor specificity that improved long-term overall survival in mice. Our data support a pathogenic cooperation among NF-κB-driven prosurvival, genetic instability, and immune evasion mechanisms in DLBCL and provide preclinical proof of concept for including PD-1/PD-L1 blockade in combinatorial immunotherapy for ABC-DLBCL. (Blood. 2019;133(22):2401-2412)

Introduction

Activated B-cell-like diffuse large B-cell lymphomas (ABC-DLBCLs) are aggressive mature B-cell non-Hodgkin's lymphomas that resemble the plasmablast stage of B-cell development, characterizing patients at high risk for relapse or failure to respond to R-CHOP standard of care (immunochemotherapy with rituximab plus cyclophosphamide, doxorubicin, vincristine, and prednisone).¹⁻³ Recently, genomic analyses have revealed new outcome-associated genetically defined DLBCL subgroups,^{4,5} evidencing the additional genetic complexity that underlies the transcriptionally defined classification of DLBCL into germinal center B-cell (GCB)- and ABC-like subtypes.^{6,7} Yet, many of the genetic hallmarks of ABC-DLBCL pathogenesis ultimately converge in 2 main oncogenic

pathways^{2,3,8-10}: activation of canonical NF-κB and impaired plasma cell terminal differentiation, with the latter being frequently the consequence of inactivating mutations/deletions of *BLIMP1/PRDM1*¹¹⁻¹³ or alternative genetic/epigenetic repressor mechanisms.^{13,14} Disruption of plasma cell gene signature has also been linked to FOXP1, which is an essential regulator of B-cell development¹⁵⁻¹⁷ and plasma cell programs.^{18,19}

Mutations in *TP53* are present in approximately 20% of DLBCLs^{4,20-24} and associate with poor survival in patients with DLBCL.^{20,25-27} The majority of *TP53* mutations in human DLBCL are accompanied by loss of p53 function,²⁰ where the expression of a mutant p53 protein may sometimes exert a dominant-negative

regulation over any remaining wild-type p53 or acquire new oncogenic functions.^{28–30} Even though bi-allelic *TP53* mutations are frequent in a distinct genetic subgroup of DLBCLs that show no ABC/GCB enrichment,^{4,21} alternative copy number-dependent mechanisms that affect other p53 pathway components and ultimately result in perturbed p53 signaling can be detected in 66% of newly diagnosed DLBCLs.³¹ For example, the negative modulator of p53 transcriptional activity, *BCL2L12* (at 19q13.42), is amplified in a subset of DLBCLs,^{4,31} mainly comprising ABC-DLBCL cases with cosegregated alterations in *PRDM1/NF-κB* modifiers and the highest contribution of activation-induced deaminase (AID)-driven signatures.⁴ Furthermore, mutated *TP53* is a predictor of refractoriness or early relapse in DLBCL.^{32,33} Therefore, it is reasonable to expect that a fully functional p53 pathway is critical in all DLBCL types, and identification of novel therapeutic vulnerabilities will benefit from deeper understanding of the pathogenic cooperation among perturbed p53 signaling, aberrantly active NF-κB, and blockade of terminal B-cell differentiation in ABC-DLBCL.

Furthermore, it is becoming increasingly evident that DLBCL comprises not only the malignant large B cells but also a complex tumor microenvironment (TME) that may play a role in DLBCL progression and response to therapy.³⁴ Negative selection checkpoints are required for removing autoreactive or aberrant GCBs,^{35,36} and it has been proposed that acquired somatic mutations harbored by malignant cells may remodel the TME and support survival.³⁴ Here, we have explored the cross talk of genetic and TME deregulated mechanisms in the pathogenesis of DLBCL, unraveling NF-κB-driven molecular addictions and immunosuppressive signatures associated with responsiveness to immunotherapy in ABC-DLBCL.

Methods

Genetically modified mice

Mouse strains were obtained from the Jackson Laboratory, including *p53^F*, *Blimp1^F*, *IKK2caGFP^{stopF}*, *Cy1-cre*, and *eYFP^{stopF}*. See supplemental Methods, available on the Blood Web site, for detailed information about strains, housing, immunizations, in vivo immunotherapy, and echography imaging. All animal care and procedures were approved by the Ethical Committee of Animal Experimentation of the University of Navarra and the Instituto de Salud Pública y Laboral de Navarra Health Department.

Human samples, primary cells, and cell lines

Normal fresh human tonsils and formalin-fixed paraffin-embedded samples from patients with DLBCL were studied with the approval of the Clinical Research Ethics Committee of the Clinica Universidad de Navarra and in accordance with ethical guidelines at the University Hospital of Katholieke Universiteit Leuven. See supplemental Methods for additional information regarding fresh cellular sorting, culture conditions of lymphoma cell lines, and the National Center for Biotechnology Information Gene Expression Omnibus data sets reanalyzed here.

Immunohistochemistry

Pathological analyses were performed using standard procedures and our previous experience,³⁷ as detailed in supplemental Methods.

Transcriptomics and ChIP-seq analyses

Information regarding quantitative real-time polymerase chain reaction (qRT-PCR), RNA-seq, RNA interference, microarray expression, murine variable diversity joining (VDJ)-immunoglobulin heavy chain (IgH)-seq,³⁸ and chromatin immunoprecipitation (ChIP)-seq, is detailed in supplemental Methods.

Flow cytometry and t-SNE analysis

Flow-based studies of surface and intracellular markers, gating strategies, Rphenograph clustering method, and t-distributed stochastic neighbor embedding (t-SNE) analysis were performed as detailed in supplemental Methods.

Statistical analyses

Statistical analyses were performed using GraphPad Prism v7.0 and are described in supplemental Methods.

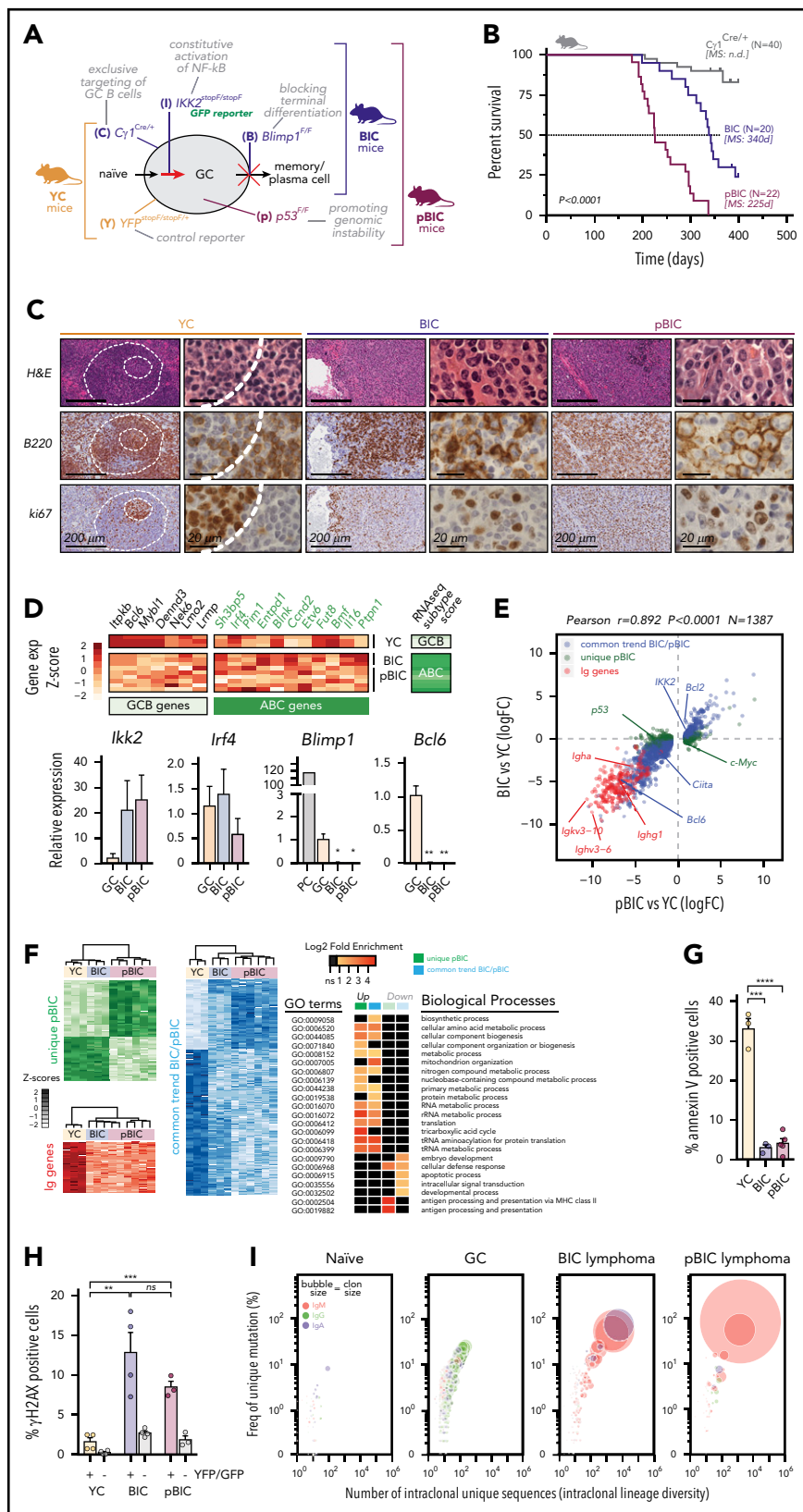
Results

p53 surveillance protects GCBs from ABC-DLBCL lymphomagenesis induced by NF-κB activation and *Blimp1* loss

Mice bearing compound mutations driving blockade of plasma cell terminal differentiation (by conditional deletion of *Blimp1*) and activation of canonical NF-κB (by conditional expression of IKK2ca, a constitutively active mutant form of IKK2) had been shown to develop lymphomas that resemble human ABC-DLBCL.⁹ Recurrently, a third oncogenic pathway is thought to promote additional genomic instability through impaired p53 signaling.^{21–23,31} To investigate the pathogenic cross talk of these 3 pathways, we crossed mice bearing conditional alterations in homologs of key human ABC-DLBCL mutations *p53^{F/F}*, *Blimp1^{F/F}*, *IKK2caGFP^{stopF/stopF}*, and used the *Cy1-Cre* to target conditional mutagenesis at early stages of the germinal center (GC) reaction (designated p, B, I, and C, respectively; Figure 1A).

To investigate whether the IKK2-mediated constitutive activation of canonical NF-κB affected p53 in GC-derived B-cell lymphomas, we first examined p53 levels in the previously described mouse model that develop ABC-DLBCL⁹ (referred to as *Blimp1^{F/F}/IKK2caGFP^{stopF/stopF}Cy1^{Cre/+}* [BIC] mice). These BIC lymphomas showed stabilization of the p53 protein (supplemental Figure 1A), as well as increased transcriptional p53 levels compared with normal GC cells (supplemental Figure 1B), suggesting ongoing DNA damage responses in the tumors. To further investigate the role of p53 in ABC-DLBCL progression, we conditionally deleted *Trp53* in the multilesion BIC background (referred as pBIC mice; Figure 1A). These novel p53-deficient pBIC mice developed an ABC-DLBCL-like phenotype that was significantly more aggressive than the p53-proficient BIC mice (Figure 1B). In particular, pBIC mice exhibited more dramatic splenomegaly (supplemental Figure 1C) and malignant expansion of GFP⁺ lymphoma B cells (supplemental Figure 1D), corresponding to large cells (supplemental Figure 1E) that could not terminally differentiate into plasma cells (supplemental Figure 1F), and exhibited a B220⁺CD38⁺CD138[–]IgM⁺ immunophenotype (supplemental Figure 1G–I). Histologic examinations of splenic tumors showed morphological features resembling human DLBCL, characterized by disrupted architecture and a diffuse growth pattern of B220⁺ki67⁺ cells (Figure 1C). Consistently, a previously validated human RNA-seq-based subtype

Figure 1. Conditional deletion of p53 cooperates with constitutive canonical NF- κ B and Blimp1 loss in ABC-DLBCL lymphomagenesis. (A) Schematic diagram of the mutant mice and targeted B-cell functions used in this study. YC controls, $YFP^{stopF/F} Cy1^{Cre/+}$; BIC, $Blimp1^{F/F} IKK2ca^{stopF/stopF} Cy1^{Cre/+}$; pBIC, $p53^{F/F} BIC$. (B) Overall survival of control or multilesson mice. (C) Representative immunohistochemical staining of hematoxylin and eosin, B220 and ki67 to label proliferating B cells in normal splenic GCs and murine diffuse B-cell lymphomas. Scale bars, 200 or 20 μ m, as indicated. (D) RNA-seq gene expression classifier distinguishes ABC-DLBCL subtype in the murine lymphomas, which is confirmed by qRT-PCR of FACS-sorted reporter-positive normal GCBs or PCs, and lymphoma B cells ($n \geq 3$ animals). Relative values are normalized to GCB expression levels. (E) Scatter plot of differentially expressed genes ($N = 1387$) as measured by RNA-seq from GFP $^+$ /YFP $^+$ reporter splenic B cells, showing log₂ fold-changes in lymphoma relative to normal GCBs ($n \geq 3$ animals). Genes were stratified and colored according to whether they were found in both lymphoma models or differentially expressed in the more aggressive pBIC model. (F) Heat maps of gene expression levels (left) and gene ontology (GO) analysis (right) for the categories of differentially expressed genes stratified in panel E. (G) Comparative percentages of apoptotic cells within reporter-positive control or lymphoma cells. (H) Comparative percentages of reporter-positive B cells that are positive for γ H2AX by intracellular FACS. Gray bars represent YFP/GFP-negative normal cells from the same tumors. (I) Bubble plot illustrating the enrichment of VDJ-IgH clonal groups within reporter-positive murine control or lymphoma cells that accumulate unique somatic mutations (y-axis) in intraclonally diverse V sequences (x-axis). Bubble sizes represent the abundance of clonal barcoded single-molecule, and therefore clon size, whereas colors indicate the dominant isotype.



classifier³⁹ distinguished the ABC-DLBCL phenotype in these murine tumors (Figure 1D, top), whereas qRT-PCR further confirmed the high expression of *Ik2k* and *Irf4* levels, as well as the loss of *Blimp1* and *Bcl6* expression (Figure 1D, bottom).

Furthermore, hemizygous expression of *IKK2ca* resulted in delayed tumor onset and death in pBIC mice (supplemental Figure 2), indicating that p53-deficient lymphoma cells rely, at least in part, on the levels of active NF- κ B signaling for

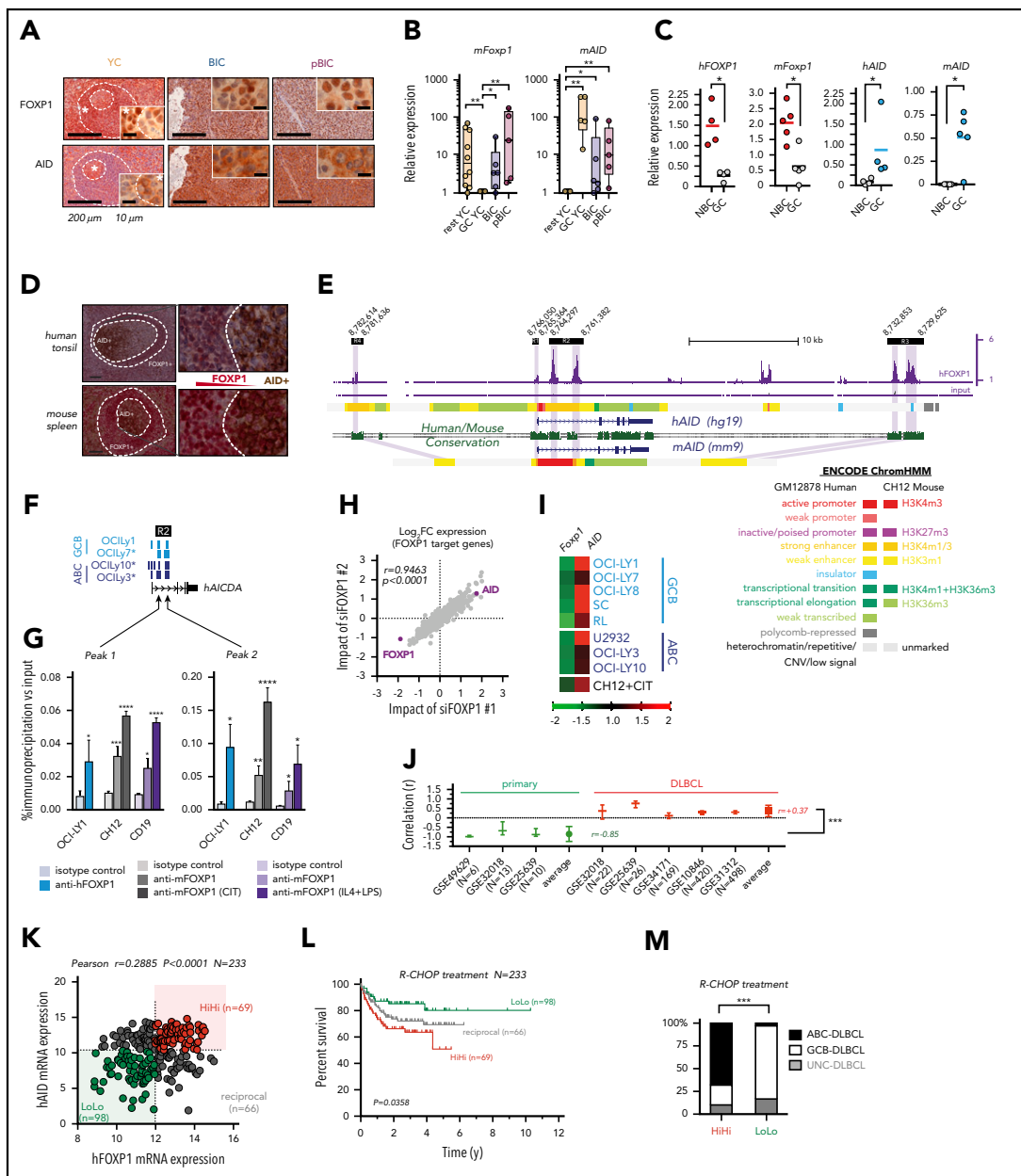


Figure 2. Aberrant coexpression of FOXP1 and AID characterizes NF-κB-driven murine and human ABC-DLBCL. (A) Representative immunohistochemical staining of FOXP1 (nuclear) and AID (cytoplasmic) in normal splenic GCs and lymphomas. Scale bars, 200 μm or 10 μm at insets. (B) Expression analysis by qRT-PCR of FACS-sorted reporter-positive normal resting or GCBs, and lymphoma B cells ($n \geq 5$ animals). Relative values were normalized to resting or GCB expression levels for *mFoxp1* or *mAID*, respectively. (C) Expression analysis by qRT-PCR of paired NBC or GCBs magnetically sorted from human tonsils or FACS sorted from normal murine spleens ($n \geq 4$). Relative values are normalized to endogenous levels *h/mGAPDH*. (D) Representative images of inverse correlation of FOXP1 and AID expression in reactive human tonsil or murine spleen examined by IHC, using combined labeling of anti-FOXP1 (brown) and anti-AID (red). Scale bars, 200 μm; magnification, $\times 20$. (E) ChIP-seq data from OCI-Ly1 cells showing enrichment of FOXP1 on the *hAID* locus. Distribution of FOXP1 occupancy is overlapped with chromatin-state models predicted by ENCODE ChromHMM from GM12878 (human B lymphoblastoid) or CH12 (mouse B-cell lymphoma) cells, and with the predicted conserved *mAID* gene locus according to Genome Browser comparison of hg19 and mm9 sequence data. Black boxes on top indicate genomic regions (R1-R4) associated with transcriptional regulation of AID expression. (F) Comparison of hFOXP1 ChIP-seq peaks at intronic region 2 of the *hAID* locus observed here in OCI-Ly1 cells or previously in other GCB-DLBCL or ABC-DLBCL cell lines (GSE69009). (G) Validation of FOXP1 occupancy at *AID* intronic peaks and measured by ChIP-qPCR in human OCI-Ly1 DLBCL cells, as well as in resting or activated murine cells (ie, CH12 lymphoma cells and primary magnetically sorted CD19⁺ splenic cells). CIT, combination of anti-CD40 plus IL-4 and TNF-β; LPS, lipopolysaccharides. (H) Scatter plot of gene expression array data from OCI-Ly1 cells showing average \log_2 fold-changes ($n = 3$ replicates) in the expression of FOXP1-bound genes (according to ChIP-seq data from OCI-Ly1) relative to scramble control after FOXP1 silencing with 2 different siRNAs. (I) Heat map of average fold-changes ($n = 3$ replicates) in the expression of FOXP1 and *AID* relative to scramble control after FOXP1-mediated silencing of *AID* in DLBCL cell lines and in CIT-activated CH12 cells. (J) Forest graph plot of Pearson r coefficients measuring the correlation of *hFOXP1* and *hAID* expression in previously published GSE series. (K) Scatter plot of FOXP1 and *AID* gene expression array data from R-CHOP-treated patients with DLBCL ($n = 233$, GSE10846). Median expression levels for FOXP1 (223287_s_at) and *AID* (219841_at) are indicated and were used as cutoff values for patient stratification. (L) Overall survival of R-CHOP-treated patients with DLBCL stratified by FOXP1/*AID* expression levels in panel K. COO subtypes were defined by expression signatures and were available in metadata from GSE10846. (N) Scatter plot of FOXP1 and *AID* protein expression data as measured by IHC scoring from CHOP-treated patients with DLBCL ($n = 112$). Median IHC scores are indicated and were used as cutoff values for patient stratification. (O) Overall survival of CHOP-treated patients with DLBCL stratified by FOXP1/*AID* IHC scores in panel N. COO subtypes were defined by the Hans IHC algorithm. HiHi, FOXP1^{high}/*AID*^{high}; LoLo, FOXP1^{low}/*AID*^{low}; NBC, naive B cells; UNC, unclassified.

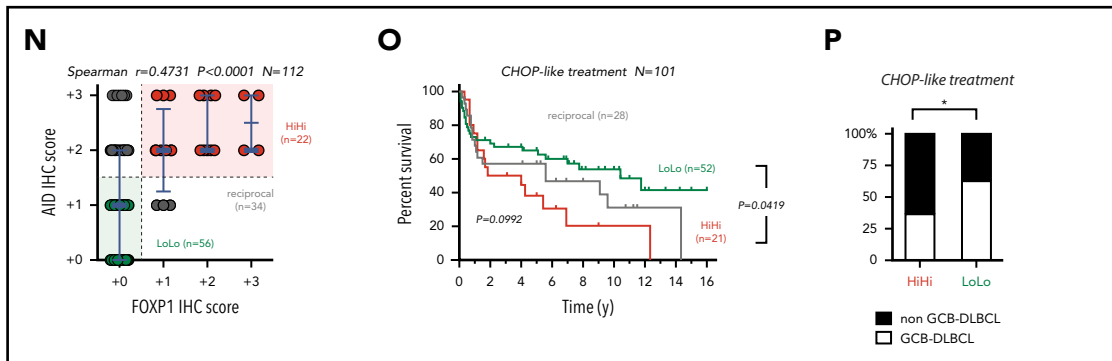


Figure 2. (Continued).

tumor progression. Altogether, these results evidence a pathogenic cooperation between p53 loss and NF- κ B activity, and suggest that p53 surveillance constitutes a main barrier to NF- κ B-driven transformation of GCBs that fail to terminally differentiate.

Aberrant coexpression of FOXP1 and AID characterizes murine and human ABC-DLBCL

Next, we analyzed the transcriptional profile of BIC and pBIC tumors by RNA-seq (Figure 1E; supplemental Table 1). Both p53-proficient and p53-deficient murine ABC-DLBCLs demonstrated strong transcriptional similarity and loss of BCR diversity, indicating clonal enrichment. Upregulated genes revealed marked enrichment of metabolic and translation processes (Figure 1F), likely facilitating tumor growth. In contrast, down-regulated genes appeared mainly enriched in processes related to development, intracellular signaling, or apoptosis (Figure 1F), which was consistent with the decreased cell death observed in these tumors (Figure 1G). We observed that murine ABC-DLBCL lymphomas accumulated high levels of unrepaired double-strand DNA breaks marked by γ -H2AX compared with control GCBs or normal lymphocytes from the same tumors (Figure 1H), and the archetypical IgH:cMyc translocation that is found in 5% to 15% of patients with DLBCL^{40,41} could be observed in the group of p53-deficient mice (supplemental Table 2). Although different mechanisms may be at the origin of chromosomal translocations in lymphoid malignancies,⁴² it is known that AID deregulation may lead to reciprocal chromosome translocations, including IgH:cMyc, facilitating the transformation of p53-deficient cells.^{43,44} Deep sequencing of murine lymphoma VDJ-IgH repertoires confirmed the strong clonal enrichment predicted by RNA-seq and demonstrated accumulation of additional somatic hypermutation (SHM) diversity compared with normal GCBs and unmutated resting B cells (Figure 1I; supplemental Table 3), suggesting the presence of ongoing AID activity in both p53-proficient and p53-deficient tumors. Moreover, we identified an aberrant coexpression of FOXP1 and the mutagenic enzyme AID in both BIC and pBIC lymphomas compared with normal GC or naive B cells from sheep red blood cells-immunized YFP^{stop/+}/C γ 1^{Cre/+} (YC) control mice (Figure 2A-B; supplemental Table 4). Indeed, human tonsils and normal murine spleens confirmed the reciprocal expression of FOXP1 and AID during the GC transit of B cells (Figure 2C-D).

FOXP1 binding was detected by ChIP-seq (Figure 2E; supplemental Table 5) in all 4 previously known regulatory regions within the AID locus,⁴⁵ which are well conserved between human and mice, and are predicted to insulate or modulate enhancer

activity by ChromHMM analysis in available human and mouse ENCODE data (Figure 2E). Of note, both ABC- and GCB-like DLBCL human cell lines demonstrated direct binding of FOXP1⁴⁶ downstream of AID TSS at 2 discrete intronic peaks (Figure 2F). This FOXP1-to-AID locus binding was already evident in murine primary CD19⁺ resting B cells and the B-cell lymphoma CH12 cells that can be activated in vitro to induce AID expression, and significantly increased on cytokine stimulation (Figure 2G), suggesting a modulated commitment of FOXP1 in the insulation of the AID locus. Consistently, siRNA-mediated silencing of hFOXP1 followed by microarray mRNA profiling in DLBCL cells (Figure 2H), or by qRT-PCR in a cohort of mouse and human lymphoma cell lines (Figure 2I), demonstrated upregulation of AID in all scenarios. In contrast, multiple human DLBCL data sets revealed a consistent reversion of the negative correlation normally observed in primary samples (Figure 2J). A clinical relevance for FOXP1/AID aberrant coexpression was further supported when the concurrence of these 2 factors was analogously evidenced in retrospective analysis of human primary DLBCL samples (Figure 2K-N; supplemental Figure 3), and found that this was associated with reduced overall survival in R-CHOP and CHOP-treated patients with DLBCL (Figure 2L,O), predominantly of the ABC subtype (Figure 2M,P). These observations suggest that constitutive NF- κ B and pro-oncogenic FOXP1 may cooperate with AID-triggered mutagenesis to promote ABC-DLBCL pathogenesis.

Mechanisms of immune evasion facilitate ABC-DLBCL tumor progression

B cells are themselves antigen-presenting cells that express major histocompatibility complex class II (MHC-II),⁴⁷ and loss of MHC-II expression characterizes ABC-DLBCL.⁴⁸ Consistently, RNAseq showed that MHC-II transactivator Ciita was significantly downregulated in both BIC and pBIC murine lymphomas (Figure 3A), which might impair T-cell activation. This was accompanied by a general trend toward loss of MHC-II gene expression (Figure 3B), which was most clear in p53-deficient lymphomas, in line with previous evidence for a link between p53 and MHC-I/II expression.^{49,50} Indeed, GO analysis revealed that antigen presentation via MHC-II was a biological process significantly downregulated in p53-deficient pBIC tumors (Figure 1F). To further investigate immunosurveillance in these NF- κ B-driven lymphomas, we measured PD-L1 levels by flow cytometry and observed a clear increase of PD-L1 in the surface of the GFP⁺ lymphoma cells from both BIC and pBIC mice compared with GCB counterparts from YC control mice (Figure 3C). These results resembled human ABC-DLBCL primary lymphomas, which

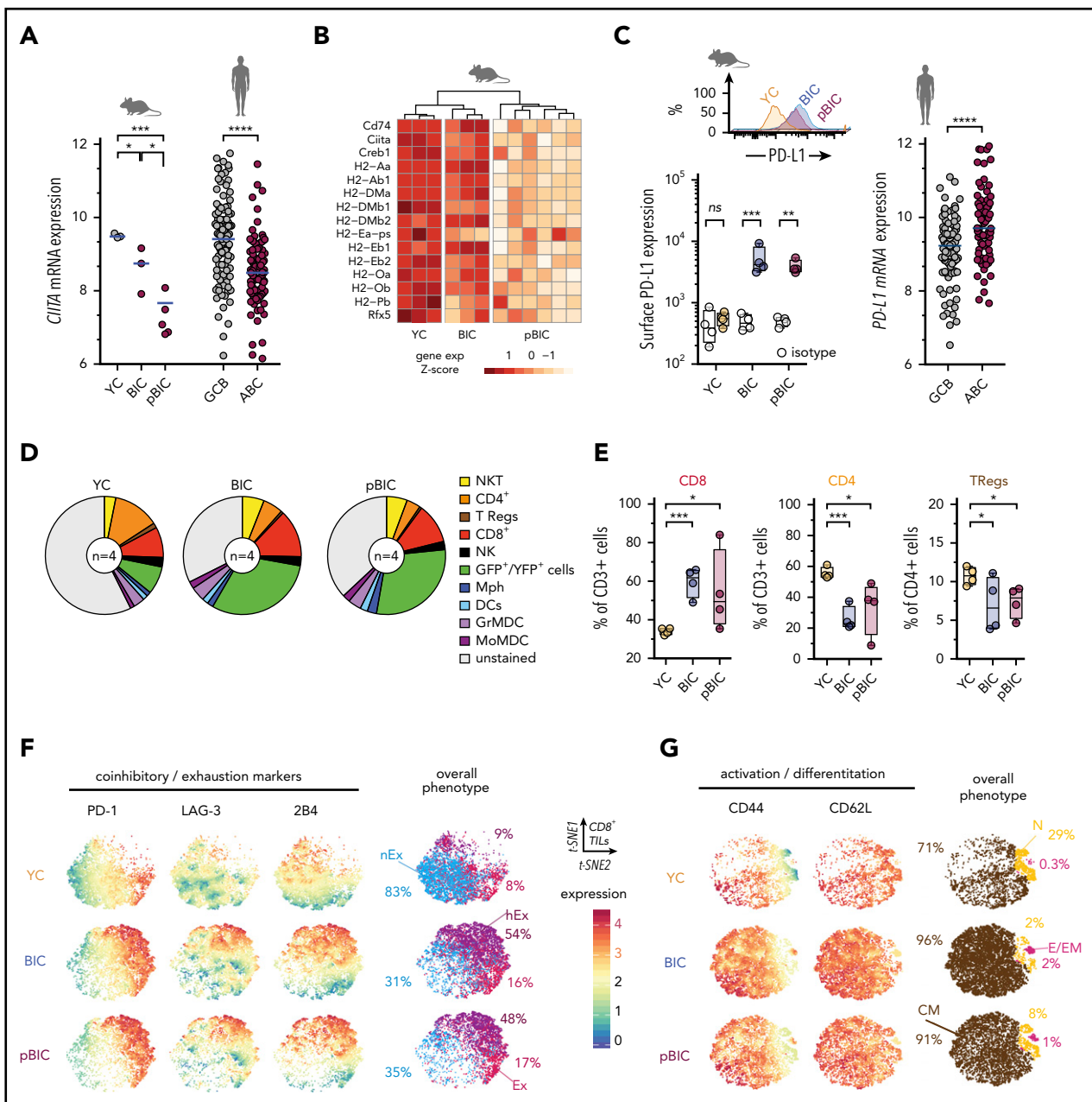


Figure 3. Decreased MHC-II gene expression and immune checkpoint deregulation cooperate with ABC-DLBCL genetic hallmarks to promote immune evasion. (A) Comparative gene expression levels of the MHC-II transactivator *CITA* in GFP⁺/YFP⁺ reporter murine B cells from control or tumoral spleens (left) and human DLBCL (right, GSE10846). (B) Heat map of gene expression levels for MHC-II genes (KEGG pathway mmu04612) in GFP⁺/YFP⁺ reporter murine B cells from control or tumoral spleens. (C) Representative FACS histograms and comparative levels of surface PD-L1 in GFP⁺/YFP⁺ reporter murine B cells (left), and *PD-L1* gene expression levels in human DLBCL (right, GSE10846). (D) Pie charts showing average percentages ($n = 4$ animals) of different immune cells in the control or tumoral spleens. (E) Comparative percentages of different T-cell populations in the control or tumoral spleens of indicated mice. (F–G) Multidimensional depiction by t-SNE of surface marker levels in aggregated total CD8⁺ T cells (dots) from control or tumoral spleens ($n = 4$ animals). Expression by FACS of coinhibitory and exhaustion markers (F) or activation and differentiation markers (G) were overlaid onto the overall t-SNE maps. Interpretation of the overall phenotype for each CD8⁺ T cell is color coded and annotated as nonexhausted (nEx; PD-1^{neg}LAG-3^{neg}2B4^{neg}), exhausted (Ex; PD-1^{hi}), hyperexhausted cells that coexpress multiple inhibitory receptors besides PD-1 (hEx), naive (N; CD44^{low}CD62L⁺), central memory (CM; CD44^{high}CD62L⁺), and effector or effector memory (E/EM; CD44^{high}CD62L^{neg}). Percentages indicate average abundance of CD8⁺ T cells with the different exhaustion/differentiation phenotypes in YC control spleens or BIC/pBIC lymphomas.

also showed increased *PD-L1* expression and loss of MHC-II transactivator *CITA* expression compared with GCB-DLBCL cases (Figure 3A,C).

The imbalance of immune cell populations in the TME of murine ABC-DLBCLs may provide an additional explanation for tumor progression. Although the myeloid compartment did not exhibit

evident relative changes compared with control YC spleens (Figure 3D; supplemental Figure 4A), the expansion of GFP⁺ lymphoma B cells was accompanied by a significant enrichment of CD8⁺ cells at the expense of CD4⁺ and CD25⁺FOXP3⁺ T regulatory cells (Figure 3E). Consistent with our hypothesis that infiltrating effector CD8⁺ cells became progressively exhausted through interaction with tumor PD-L1⁺ cells, most CD8⁺ T cells

upregulated 1 or multiple inhibitory receptors including PD-1, LAG-3, and 2B4 (Figure 3F), which would decrease T-cell cytotoxicity against tumor cells.⁵¹ Therefore, this immune checkpoint phenotype in murine ABC-DLBCLs recapitulates the positive correlation between PD-L1 expression in the lymphoma cells and the presence of PD-1⁺ tumor-infiltrating lymphocytes (TILs) that has been observed in some human DLBCL studies.⁵²⁻⁵⁴ Furthermore, most tumor-associated CD8⁺ TILs coexpressed both CD44 and CD62L markers (Figure 3G), which are indicative of central memory phenotypes⁵⁵ and suggest that these are tumor cognate cells with the potential to be reactivated. All these observations support the notion that typical ABC-DLBCL genetic alterations can ultimately cross talk with the TME to promote T-cell dysfunction through PD-L1/PD-1 signaling and weaken antigen presentation, therefore facilitating tumor immune evasion.

Immune checkpoint PD-1 blockade enhances anti-CD20 efficacy in the mouse ABC-DLBCL-like model

The presence of PD-1⁺ TILs is observed in 40% to 60% of human DLBCLs, even though its clinical value is still controversial.⁵⁴ This prompted us to investigate whether our murine model system might support a predictive value of PD-L1⁺ tumor cells and PD-1⁺ TILs as biomarkers for successful combinational immunotherapy responses in ABC-DLBCL. A recent phase 2 study with anti-PD-1 monotherapy (Nivolumab)⁵⁶ has shown low overall response rates in relapsed/refractory DLBCL, but there is limited information about the efficacy of PD-1 in combination with anti-CD20 immunotherapy in DLBCL. Therefore, we hypothesized that targeting DLBCL tumors with anti-CD20 monoclonal antibodies (mAbs) and simultaneous immune checkpoint blockade might be efficacious and tolerable. Combination immunotherapy with anti-CD20 and anti-PD-1 was superior to either monotherapy in overall survival responses, even though no significant improvement could be observed with the single anti-PD-1 regimen (Figure 4A). Consistently, ultrasound transversal measurements of the spleen during the first 3 cycles of treatment demonstrated that anti-CD20 as monotherapy or in combination was able to reduce the splenomegaly associated with the pBIC DLBCL, which was not evident with anti-PD-1 alone (Figure 4B).

To further investigate how the immunological landscape responded to these immunotherapy combinations, tumor spleens treated for 4 weeks were subjected to immune cell analysis. After anti-CD20 treatment, either as monotherapy or in combination with PD-1 blockade, we could observe a substantial depletion of GFP⁺ lymphoma B cells by immunohistochemistry (IHC; Figure 4C) or by fluorescence-activated cell sorting (FACS; Figure 4D). In addition, although anti-PD-1-alone or anti-CD20-alone treatment of lymphomas had limited effect, the combination of anti-CD20/anti-PD-1 displayed major changes in splenic cell populations (Figure 4E; supplemental Figure 4B). Of note, the overall population of CD3⁺ cells, including NKT, CD4⁺, T regulatory cells, and CD8⁺ cells, was markedly enriched in the anti-CD20/PD-1 combo immunological landscape, evidencing a distinctive T-cell-inflamed microenvironment that might promote extended therapeutic protection after treatment. Indeed, the combo treatment sustained a trend toward the clearance of PD-1⁺ T cells in the spleen (Figure 4F), in favor of CD8 and CD4 populations with absence or low levels of coinhibitory receptors PD-1, LAG3, or

2B4 (Figure 4G, top). Furthermore, these T cells preferentially expressed CD44 receptors, and although CD8 T cells conserved their prevalent initial central memory phenotype (CD44⁺CD62L⁺), new infiltrating CD4 T cells exhibited effector memory (CD44⁺CD62L⁻) phenotypes (Figure 4G, bottom), supporting the notion that an anti-CD20/anti-PD-1 combination was most efficient at establishing an overall activated T-cell microenvironment in the spleen. Consistent with this, maintained depletion of CD8 or CD4 T cells abrogated the survival benefit of combined immunotherapy in pBIC mice (supplemental Figure 5), indicating that T-cell-related immune-regulatory mechanisms mediate therapeutic effects in this ABC-DLBCL preclinical model.

Reinvigoration of the exhausted TILs was parallel to the specific destruction of PD-L1⁺CD19⁺GFP⁺ lymphoma B cells, whereas neighbor normal B cells remained largely negative for PD-L1 and were refractory to anti-PD-1 effects, succumbing only to the unspecific pan-B cytotoxicity of anti-CD20 mAbs (Figure 4H). These observations prompted us to consider that antitumor specificity contributed to the anti-CD20/anti-PD-1 combination benefit, as treatment with anti-PD-1 mAbs exclusively affected GFP⁺ lymphoma cells, whereas anti-CD20 treatment was non-selective in eliminating virtually all normal and tumoral B cells from the spleen (Figure 4I). In fact, incipient antitumoral responses with more reticular GFP⁺ dispersion and enlarged CD4/CD8 T-cell areas could be already observed on anti-PD-1 treatment, which was far more evident in the combination treatment (Figure 4C). Indeed, this specific antitumoral activity triggered by anti-PD-1 had some effect by itself on the overall depletion of GFP⁺ lymphoma B cells (Figure 4D), although it failed to significantly improve overall survival and tumor regression (Figure 4A-B), indicating that the more dramatic B-cell depletion mediated by anti-CD20 maximizes the effect of PD-1 blockade. Furthermore, we observed that anti-PD-1 administration conferred extended protection against the relapse of GFP⁺ malignant B cells on full depletion of CD20⁺ B cells, whereas it preserved the desirable normal B-cell reappearance (Figure 4J). All together, these results are consistent with the better long-term survival responses observed in the combination treatment, supporting our hypothesis that immune checkpoint blockade cooperates with the direct depletion of GFP⁺CD20⁺ lymphoma cells.

Discussion

The combination of constitutively active IKK2 with biallelic inactivation of *Blimp1* and *Trp53* in the GCBs of pBIC mice represents a genetic background that models the predicted effects of multiple combinatorial somatic mutations and copy-number alterations that are found in human DLBCL, and ultimately converge in 3 ABC-DLBCL hallmark pathways: constitutive activation of canonical NF-κB, blockade of terminal differentiation, and perturbation of p53 signaling. In full accord with the results of Calado et al,⁹ canonical NF-κB and Blimp1 loss (the BIC mice) cooperate to promote ABC-DLBCL. However, the long latency and the increased p53 expression in the oligoclonal tumors from these mice suggested that p53 surveillance is a main barrier for the pathogenesis of this disease. Indeed, we found that conditional deletion of p53 in mouse GCBs strongly synergized with IKK2 activation and Blimp1 loss to promote GC-derived lymphomagenesis. Thus, our work suggests that additional oncogenic events are required for NF-κB-driven transformation of GC-experienced plasmablasts that fail to terminally differentiate,

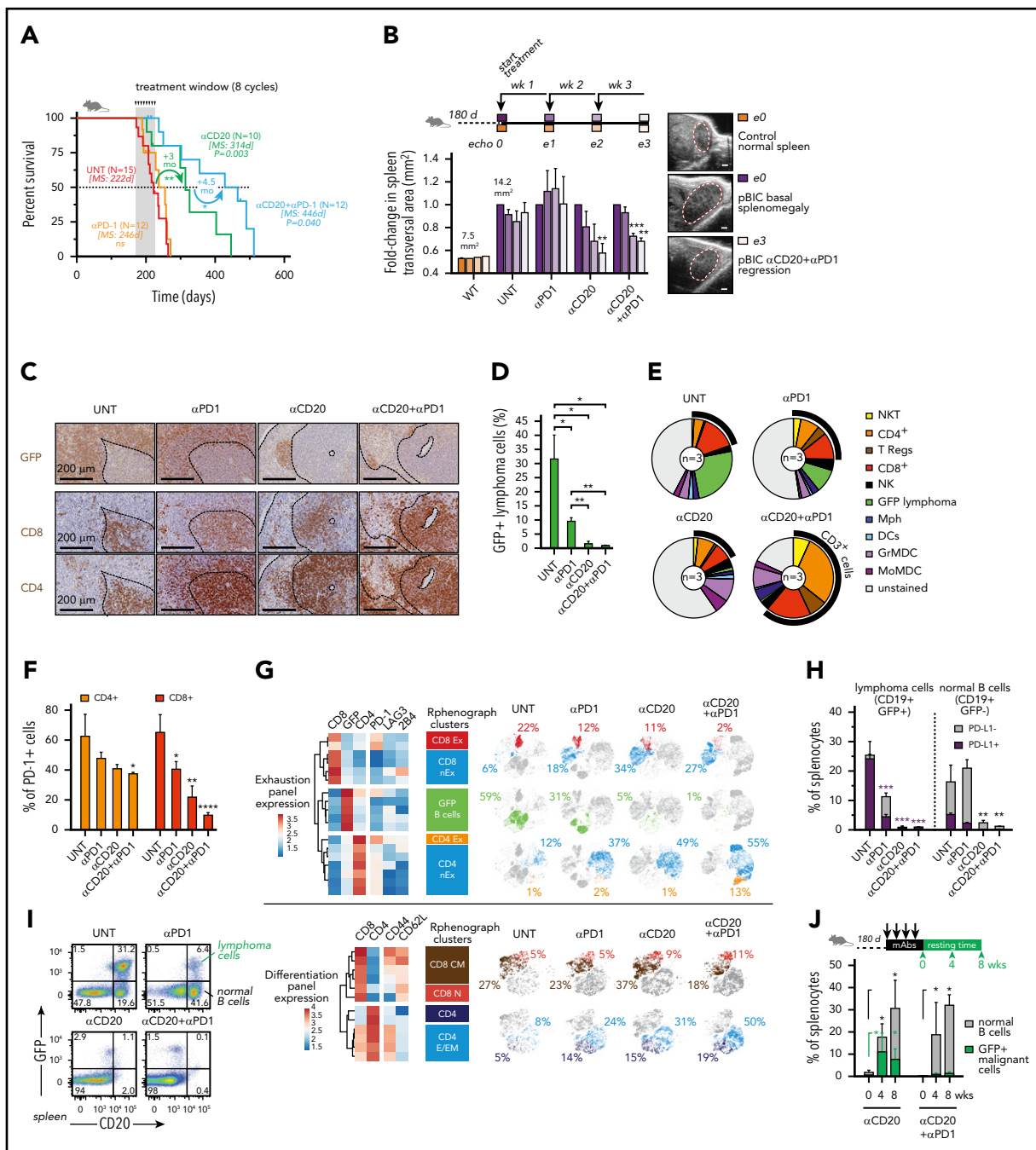


Figure 4. Immunotherapy with anti-PD-1 enhances anti-CD20 efficacy in the aggressive immunocompetent ABC-DLBCL mouse model. (A) Overall survival of murine ABC-DLBCL pBIC mice treated with different immunotherapy combinations. (B) Relative changes in splenic transversal areas measured by ventral ultrasound of pBIC mice (>180 days, with evidence of splenomegaly, n = 3) at 4 sequential times during immunotherapy treatment, as indicated in the scheme at the top. Representative ultrasound sections of the spleen are shown on the right. Scale bars, 1 mm. (C) Representative immunohistochemical staining of GFP, CD4, and CD8 to label T-cell infiltration in murine pBIC lymphomas (>180 days) that had received 4 weeks of immunotherapy. Scale bars, 200 μm . (D) Comparative percentages of splenic B220⁺ GFP⁺ lymphoma cells from pBIC lymphomas (>180 days) in response to different 4-week immunotherapy regimens (n \geq 3). (E) Pie charts showing percentages of immune cells in the spleen pBIC mice (>180 days) after 4-week immunotherapy (n = 3). (F) Comparative fractions of PD-1-positive T cells in the TME of pBIC mice (>180 days) after 4-week immunotherapy (n = 3). (G) Heat maps of mean expression intensity of coinhibitory/exhaustion (top) and activation/differentiation (bottom) surface markers within lymphocyte subsets detected by Rphenograph clustering (n = 3 mice \times 4 groups). Distribution of these cell populations in response to 4-week immunotherapy (n = 3) is represented in t-SNE maps and colored. Percentages indicate average abundance of each cell population in the corresponding treatment group. (H) Comparative fractions of PD-L1-positive or PD-L1-negative cells within the compartment of lymphoma cells (CD19⁺ GFP⁺) or neighbor normal B cells (CD19⁺ GFP⁻) from pBIC mice (>180 days) after 4-week immunotherapy (n = 3). (I) FACS analysis to assess the specific depletion of lymphoma or normal B cells in the spleen of pBIC mice (>180 days) after 4-week immunotherapy (n = 3). (J) Percentages of reappearing splenocytes (CD20⁺ GFP⁺) or neighbor normal B cells (CD20⁺ GFP⁻) during a resting period of 8 weeks after anti-CD20-based immunotherapy that can efficiently deplete the B-cell compartment in pBIC mice (>180 days, n = 3). MS, median survival; UNT, untreated.

which are initially resolved by a proficient p53 DNA damage response pathway.

In the search for major NF- κ B downstream players that may promote genomic instability and contribute to ABC-DLBCL progression, we identified an aberrant coexpression of the transcription factor FOXP1 and the mutagenic enzyme AID. A relevance for this positive correlation was further supported when the concurrence of these 2 factors was similarly evidenced in retrospective collections of human primary DLBCL samples, showing association with reduced overall survival and the ABC subtype. Expression of FOXP1 might be promoting DLBCL survival by diverse mechanisms, including potentiation of the Wnt/b-catenin signaling⁵⁷ or repression of pro-apoptotic genes,^{18,46,58} which is consistent with the decreased apoptosis that we observed in the murine ABC-DLBCLs. Upregulation of FOXP1 was expected, as it is broadly recognized as a prognostic indicator and biomarker for human ABC-DLBCL.⁵⁹⁻⁶¹ In fact, NF- κ B activation through IKK2 has been shown to cooperate with FOXP1 to promote lymphoma survival.⁴⁶ However, the presence of AID and ongoing SHM in the tumors were unanticipated, as we had initially predicted that these would be suppressed in the presence of FOXP1 because we and others have shown that FOXP1 is a transcriptional repressor during the GC reaction that can bind AID and other GC-related genes.^{17,18,61} Indeed, we confirmed the reciprocal expression of FOXP1 and AID during the GC transit of B cells in human tonsils and normal murine spleens, and found a direct binding of FOXP1 downstream of AID TSS at 2 discrete intronic peaks, which exhibited strong enhancer chromatin marks and had been previously associated with ubiquitous silencers.^{45,62} However, the transcriptional repression of AID by FOXP1 results inefficient in the presence of constitutive NF- κ B activation and IRF4 expression, which characterize ABC-DLBCL and are known to be direct strong activators of AID.^{45,62-66} Our results support that AID is a bona fide target of FOXP1 repression, even though FOXP1 insulation of AID becomes inefficient in lymphoma cells with constitutive NF- κ B activity.

Tight regulation of AID in activated GCBs is necessary to maintain genomic integrity and avoid AID-driven lymphomagenesis.⁶⁷⁻⁷⁰ Indeed, evidence for AID expression and the accumulation of AID-related mutations has been observed in human DLBCL.^{24,71-73} Here, murine lymphomas accumulated high levels of unrepaired double-strand DNA breaks marked by γ -H2AX and the archetypical IgH:cMyc translocation could be evidenced in the group of p53-deficient mice. These genetic alterations might be attributable to AID off-target activity⁷⁴⁻⁷⁷ and are consistent with a role for p53 eliminating cells bearing AID-induced translocations.⁴²⁻⁴⁴ Furthermore, VDJ-IgH-seq from murine AID-positive ABC-DLBCL lymphomas, regardless of p53 deficiency, demonstrated strong clonal enrichment and accumulation of additional somatic hypermutation (SHM) diversity compared with normal GCBs and unmutated resting B cells, thus suggesting the presence of ongoing AID activity in the tumors during malignant progression. On the basis of all these observations, we postulate that constitutive expression of AID in human ABC-DLBCL cooperates with the prosurvival pressure imposed by NF- κ B activation to increase genomic instability and accelerate lymphoma evolution, especially in malignant cells with perturbed p53 signaling.

Finally, we could confirm a cross talk of the malignant DLBCL cells with the TME to enable immune evasion. Both murine ABC-DLBCL-like models (BIC/pBIC) demonstrated a function of

constitutive canonical NF- κ B activation and *Blimp1* loss in promoting T-cell dysfunction in DLBCL through upregulation of PD-L1 and loss of MHC-II gene expression. The most clear downregulation of MHC-II genes was associated with the perturbation of p53 signaling in pBIC tumors, which might contribute at least in part to their worse outcome. Interestingly, surface or soluble PD-L1 expression⁷⁸⁻⁸² and reduced MHC-II antigen presentation^{48,83} have been linked to poor clinical outcomes and ABC-DLBCL. Furthermore, FOXP1 is a direct repressor of MHC-II genes in ABC-DLBCL,^{18,84} and NF- κ B has been shown to be important for PD-L1 expression⁸⁵⁻⁸⁷ and stabilization,⁸⁸ providing underlying mechanisms to support our observations that a constitutive NF- κ B/FOXP1 pathway cooperates with perturbed p53 signaling to promote immune escape in ABC-DLBCL. Consistent with this, tumor-infiltrating CD8 $^{+}$ T cells exhibited central memory and exhausted phenotypes, with upregulation of 1 or multiple inhibitory receptors including PD-1, LAG-3, and 2B4, which would decrease T-cell cytotoxicity against tumoral cells.^{51,55} All these observations suggest that BIC/pBIC mouse models are able to recapitulate the complex cross talk between intracellular NF- κ B activation and antitumoral immune evasion in ABC-DLBCL, becoming useful preclinical models to examine both the biology of the human disease and new therapeutic approaches.

The immune checkpoint phenotype observed here in murine ABC-DLBCLs recapitulates the positive correlation between lymphoma PD-L1 expression and the presence of PD-1 $^{+}$ TILs that has been observed in some human studies,^{52,53} supporting a predictive value of PD-L1 and exhausted CD8 $^{+}$ TILs as biomarkers for combinational immunotherapy response in ABC-DLBCL. Although the efficacy of immune checkpoint blockade varies greatly between different subtypes of lymphoma,^{54,89,90} and relapsed/refractory DLBCL has shown low response rates to anti-PD-1 monotherapy,⁵⁶ it may be hoped that some patients with lymphoma will be more likely to respond to the right combination immunotherapy. Preliminary results from combination immunotherapy targeting both CD20 and PD-1 in follicular lymphoma are encouraging (NCT02446457).⁹¹ However, it is yet unclear whether this combination may have clinical benefits in DLBCL, for the future results from ongoing trials of anti-PD-1 mAbs in combination with anti-CD20-based chemo-immunotherapy (NCT02541565, NCT03259529, and NCT03366272) that are highly expected in the future. In this context, our study provides *in vivo* preclinical evidence that PD-1 blockade cooperates with anti-CD20-mediated depletion of lymphoma cells to reshape the immunosuppressive TME and facilitate long-term antitumor responses in NF- κ B-driven p53-deficient ABC-DLBCL. Future mechanistic studies will make it possible to explore whether the *in vivo* benefit of this combination responds to interacting or completely independent mechanisms of drug action.⁹² In the p53-deficient/NF- κ B-driven mouse model for ABC-DLBCL, we observed that although anti-CD20 mAbs provide a basal robust elimination of tumor cells, simultaneous immune checkpoint blockade with anti-PD-1 mAbs confers extended antitumor efficacy by promoting immune cell infiltration, narrowing co-inhibitory signals, and unraveling long-term cognate antitumor specificity in the DLBCL tumor microenvironment. These findings support that immune checkpoints hold promising therapeutic potential in ABC-DLBCL and provide preclinical proof of concept for the clinical evaluation of incorporating anti-PD-1 to the current anti-CD20-based modalities as combination immunotherapy for ABC-DLBCL.

Acknowledgments

The authors thank Matthew D. Scharff, Silvo Conticello, and Richard Chahwan for the kind gift of cell lines and reagents; Silvestre Vicent and Vasco Barreto for access to the p53^F and eYFP^{stopF} mouse lines, respectively; Angel Panizo for pathology advice; Genentech for in vivo functional grade anti-mouse CD20 mAbs; and Kathleen Van den Eynde, Julie Morscio, Ana Zafra, Xavier Morales, and Fernando López Aznal for technical assistance. The authors are also indebted to members of animal facility, morphology unit, CIMALab Diagnostics, and University of Navarra Biobank.

This work was supported by grants from Fondo Europeo de Desarrollo Regional (FEDER)/Ministerio de Ciencia, Innovación y Universidades-Agencia Estatal de Investigación (SAF2013-45787-R, SAF2017-82309-R) and Gobierno de Navarra (GN-106/2014) and contributions from Fundación Obra Social La Caixa to S.R., who was funded as research fellow of the European Marie Curie (FP7-PIIF-2012-328177) and Ramón y Cajal programs (RYC-2014-16399), as well as from Instituto de Salud Carlos III with FEDER cofunding (CIBERONC, PI16/00581 "Una manera de hacer Europa"), Worldwide Cancer Research (WCR15-1322), and Fundacion Arnal Planelles (J.A.M.-C.). Additional funding was received from the Fondazione Umberto Veronesi (D.B.); Chemotherapy Foundation grant LLS SCOR-7012-16 and National Institutes of Health, National Cancer Institute grant R01-CA187492 (A.M.); and National Institutes of Health, National Institute of General Medical Sciences grant 1R01GM111741 and National Institutes of Health, National Institute of Allergy and Infectious Diseases grant 1R01AI132507 (T.M.).

Authorship

Contribution: J.A.M.-C. and S.R. conceived the study; M.P., J.A.M.-C., and S.R. designed experiments, analyzed data, and cowrote the manuscript; M.P., M.M.-V., E.F.R., M.-J.G.-B., and S.R. performed experiments; C.P. contributed to the design and interpretation of immunotherapy experiments; S.H.-S., D.A., N.C., and J.J.L. designed and performed the characterization of TME by cytometry and contributed to its interpretation; X.S. and O.B. performed pathological analyses; D.B.

constructed and sequenced VDJ-IgH libraries; S.M. and T.M. performed computational immunology analyses; E.G. performed bioinformatics analyses; A.S., J.I.M.-F., K.L.B., J.C., and A.M.-B. performed experiments related to FOXP1 and AID interaction; and A.M. contributed to the design and support of experiments, as well as to discussion of results.

Conflict-of-interest disclosure: The authors declare no competing financial interests.

ORCID profiles: M.P., 0000-0002-1678-1054; M.-J.G.-B., 0000-0001-6051-8475; S.H.-S., 0000-0003-3391-1516; D.B., 0000-0001-7889-8103; E.G., 0000-0003-0547-681X; J.C., 0000-0002-2017-4206; N.C., 0000-0003-3817-6434; J.J.L., 0000-0003-1641-3881; T.M., 0000-0003-0025-9285; A.M., 0000-0002-8074-2287; J.A.M.-C., 0000-0002-7938-3950; S.R., 0000-0003-1095-0715.

Correspondence: Sergio Roa, 55 Pio XII Ave, 31008 Pamplona, Spain; e-mail: sroa@unav.es; and Jose Angel Martinez-Climent, 55 Pio XII Ave, 31008 Pamplona, Spain; e-mail: jamcliment@unav.es.

Footnotes

Submitted 10 December 2018; accepted 4 April 2019. Prepublished online as *Blood First Edition* paper, 11 April 2019; DOI 10.1182/blood.2018889931.

Data discussed in this publication are accessible through Gene Expression Omnibus SuperSeries accession number GSE116290.

The online version of this article contains a data supplement.

The publication costs of this article were defrayed in part by page charge payment. Therefore, and solely to indicate this fact, this article is hereby marked "advertisement" in accordance with 18 USC section 1734.

REFERENCES

- Lenz G, Staudt LM. Aggressive lymphomas. *N Engl J Med*. 2010;362(15):1417-1429.
- Shaffer AL III, Young RM, Staudt LM. Pathogenesis of human B cell lymphomas. *Annu Rev Immunol*. 2012;30(1):565-610.
- Roschewski M, Staudt LM, Wilson WH. Diffuse large B-cell lymphoma-treatment approaches in the molecular era. *Nat Rev Clin Oncol*. 2014;11(1):12-23.
- Chapuy B, Stewart C, Dunford AJ, et al. Molecular subtypes of diffuse large B cell lymphoma are associated with distinct pathogenic mechanisms and outcomes [published correction appears in *Nat Med*. 2018;24(8):1290-1291 and *Nat Med*. 2018;24(8):1292]. *Nat Med*. 2018;24(5):679-690.
- Schmitz R, Wright GW, Huang DW, et al. Genetics and pathogenesis of diffuse large B-cell lymphoma. *N Engl J Med*. 2018;378(15):1396-1407.
- Rosenwald A, Wright G, Chan WC, et al; Lymphoma/Leukemia Molecular Profiling Project. The use of molecular profiling to predict survival after chemotherapy for diffuse large-B-cell lymphoma. *N Engl J Med*. 2002;346(25):1937-1947.
- Alizadeh AA, Eisen MB, Davis RE, et al. Distinct types of diffuse large B-cell lymphoma identified by gene expression profiling. *Nature*. 2000;403(6769):503-511.
- Rui L, Schmitz R, Ceribelli M, Staudt LM. Malignant pirates of the immune system. *Nat Immunol*. 2011;12(10):933-940.
- Calado DP, Zhang B, Srinivasan L, et al. Constitutive canonical NF-κB activation cooperates with disruption of BLIMP1 in the pathogenesis of activated B cell-like diffuse large cell lymphoma. *Cancer Cell*. 2010;18(6):580-589.
- Sehn LH, Gascoyne RD. Diffuse large B-cell lymphoma: optimizing outcome in the context of clinical and biologic heterogeneity. *Blood*. 2015;125(1):22-32.
- Pasqualucci L, Compagno M, Houldsworth J, et al. Inactivation of the PRDM1/BLIMP1 gene in diffuse large B cell lymphoma. *J Exp Med*. 2006;203(2):311-317.
- Tam W, Gomez M, Chadburn A, Lee JW, Chan WC, Knowles DM. Mutational analysis of PRDM1 indicates a tumor-suppressor role in diffuse large B-cell lymphomas. *Blood*. 2006;107(10):4090-4100.
- Mandelbaum J, Bhagat G, Tang H, et al. BLIMP1 is a tumor suppressor gene frequently disrupted in activated B cell-like diffuse large B cell lymphoma. *Cancer Cell*. 2010;18(6):568-579.
- Pasqualucci L, Dalla-Favera R. The genetic landscape of diffuse large B-cell lymphoma. *Semin Hematol*. 2015;52(2):67-76.
- Hu H, Wang B, Borde M, et al. Foxp1 is an essential transcriptional regulator of B cell development. *Nat Immunol*. 2006;7(8):819-826.
- Patzelt T, Keppler SJ, Gorka O, et al. Foxp1 controls mature B cell survival and the development of follicular and B-1 B cells. *Proc Natl Acad Sci USA*. 2018;115(12):3120-3125.
- Sagardoy A, Martinez-Ferrandis JI, Roa S, et al. Downregulation of FOXP1 is required during germinal center B-cell function. *Blood*. 2013;121(21):4311-4320.
- Dekker JD, Park D, Shaffer AL III, et al. Subtype-specific addiction of the activated B-cell subset of diffuse large B-cell lymphoma to FOXP1. *Proc Natl Acad Sci USA*. 2016;113(5):E577-E586.
- van Keimpema M, Grüneberg LJ, Mokry M, et al. The forkhead transcription factor FOXP1 represses human plasma cell differentiation. *Blood*. 2015;126(18):2098-2109.
- Xu-Monette ZY, Wu L, Visco C, et al. Mutational profile and prognostic significance of TP53 in diffuse large B-cell lymphoma patients treated with R-CHOP: report from an International DLBCL Rituximab-CHOP Consortium Program Study. *Blood*. 2012;120(19):3986-3996.
- Pasqualucci L, Trifonov V, Fabbri G, et al. Analysis of the coding genome of diffuse large B-cell lymphoma. *Nat Genet*. 2011;43(9):830-837.
- Lohr JG, Stojanov P, Lawrence MS, et al. Discovery and prioritization of somatic

- mutations in diffuse large B-cell lymphoma (DLBCL) by whole-exome sequencing. *Proc Natl Acad Sci USA*. 2012;109(10):3879-3884.
23. Morin RD, Mendez-Lago M, Mungall AJ, et al. Frequent mutation of histone-modifying genes in non-Hodgkin lymphoma. *Nature*. 2011;476(7360):298-303.
 24. Zhang J, Grubor V, Love CL, et al. Genetic heterogeneity of diffuse large B-cell lymphoma. *Proc Natl Acad Sci USA*. 2013;110(4):1398-1403.
 25. Young KH, Leroy K, Møller MB, et al. Structural profiles of TP53 gene mutations predict clinical outcome in diffuse large B-cell lymphoma: an international collaborative study. *Blood*. 2008;112(8):3088-3098.
 26. Young KH, Weisenburger DD, Dave BJ, et al. Mutations in the DNA-binding codons of TP53, which are associated with decreased expression of TRAILreceptor-2, predict for poor survival in diffuse large B-cell lymphoma. *Blood*. 2007;110(13):4396-4405.
 27. Tessoulin B, Eveillard M, Lok A, et al. p53 dysregulation in B-cell malignancies: More than a single gene in the pathway to hell. *Blood Rev*. 2017;31(4):251-259.
 28. Muller PA, Vousden KH. p53 mutations in cancer. *Nat Cell Biol*. 2013;15(1):2-8.
 29. Freed-Pastor WA, Prives C. Mutant p53: one name, many proteins. *Genes Dev*. 2012;26(12):1268-1286.
 30. Petitjean A, Mathe E, Kato S, et al. Impact of mutant p53 functional properties on TP53 mutation patterns and tumor phenotype: lessons from recent developments in the IARC TP53 database. *Hum Mutat*. 2007;28(6):622-629.
 31. Monti S, Chapuy B, Takeyama K, et al. Integrative analysis reveals an outcome-associated and targetable pattern of p53 and cell cycle deregulation in diffuse large B cell lymphoma. *Cancer Cell*. 2012;22(3):359-372.
 32. Intlekofer AM, Joffe E, Batlevi CL, et al. Integrated DNA/RNA targeted genomic profiling of diffuse large B-cell lymphoma using a clinical assay. *Blood Cancer J*. 2018;8(6):60.
 33. Morin RD, Assouline S, Alcaide M, et al. Genetic landscapes of relapsed and refractory diffuse large B-cell lymphomas. *Clin Cancer Res*. 2016;22(9):2290-2300.
 34. Scott DW, Gascoyne RD. The tumour microenvironment in B cell lymphomas. *Nat Rev Cancer*. 2014;14(8):517-534.
 35. Victora GD, Nussenzweig MC. Germinal centers. *Annu Rev Immunol*. 2012;30(1):429-457.
 36. Mayer CT, Gazumyan A, Kara EE, et al. The microanatomic segregation of selection by apoptosis in the germinal center. *Science*. 2017;358(6360):eaao2602.
 37. Robles EF, Mena-Varas M, Barrio L, et al. Homeobox NKX2-3 promotes marginal-zone lymphomagenesis by activating B-cell receptor signalling and shaping lymphocyte dynamics. *Nat Commun*. 2016;7(1):11889.
 38. Vergani S, Korsunsky I, Mazzarello AN, Ferrer G, Chiorazzi N, Bagnara D. Novel method for high-throughput full-lengthIGHV-D-J sequencing of the immune repertoire from bulk B-cells with single-cell resolution. *Front Immunol*. 2017;8:1157.
 39. Reddy A, Zhang J, Davis NS, et al. Genetic and functional drivers of diffuse large B cell lymphoma. *Cell*. 2017;171(2):481-494.
 40. Ott G, Rosenwald A, Campo E. Understanding MYC-driven aggressive B-cell lymphomas: pathogenesis and classification. *Blood*. 2013;122(24):3884-3891.
 41. Ennishi D, Mottok A, Ben-Neriah S, et al. Genetic profiling of MYC and BCL2 in diffuse large B-cell lymphoma determines cell-of-origin-specific clinical impact. *Blood*. 2017;129(20):2760-2770.
 42. Nussenzweig A, Nussenzweig MC. Origin of chromosomal translocations in lymphoid cancer. *Cell*. 2010;141(1):27-38.
 43. Robbiani DF, Bunting S, Feldhahn N, et al. AID produces DNA double-strand breaks in non-Ig genes and mature B cell lymphomas with reciprocal chromosome translocations. *Mol Cell*. 2009;36(4):631-641.
 44. Ramiro AR, Jankovic M, Callen E, et al. Role of genomic instability and p53 in AID-induced c-myc-Igh translocations. *Nature*. 2006;440(7080):105-109.
 45. Tran TH, Nakata M, Suzuki K, et al. B cell-specific and stimulation-responsive enhancers derepress Aicda by overcoming the effects of silencers. *Nat Immunol*. 2010;11(2):148-154.
 46. van Keimpema M, Grüneberg LJ, Mokry M, et al. FOXP1 directly represses transcription of proapoptotic genes and cooperates with NF-κB to promote survival of human B cells. *Blood*. 2014;124(23):3431-3440.
 47. Adler LN, Jiang W, Bhamidipati K, et al. The other function: class II-restricted antigen presentation by B cells. *Front Immunol*. 2017;8:319.
 48. Wilkinson ST, Vanpatten KA, Fernandez DR, et al. Partial plasma cell differentiation as a mechanism of lost major histocompatibility complex class II expression in diffuse large B-cell lymphoma. *Blood*. 2012;119(6):1459-1467.
 49. Wang B, Niu D, Lai L, Ren EC. p53 increases MHC class I expression by upregulating the endoplasmic reticulum aminopeptidase ERAP1. *Nat Commun*. 2013;4(1):2359.
 50. Zeki K, Tanaka Y, Morimoto I, et al. Induction of expression of MHC-class-II antigen on human thyroid carcinoma by wild-type p53. *Int J Cancer*. 1998;75(3):391-395.
 51. Chen DS, Mellman I. Elements of cancer immunity and the cancer-immune set point. *Nature*. 2017;541(7637):321-330.
 52. Kwon D, Kim S, Kim PJ, et al. Clinicopathological analysis of programmed cell death 1 and programmed cell death ligand 1 expression in the tumour microenvironments of diffuse large B cell lymphomas. *Histopathology*. 2016;68(7):1079-1089.
 53. Menter T, Bodmer-Haecki A, Dirnhofer S, Tzankov A. Evaluation of the diagnostic and prognostic value of PDL1 expression in Hodgkin and B-cell lymphomas. *Hum Pathol*. 2016;54:17-24.
 54. Xu-Monette ZY, Zhou J, Young KH. PD-1 expression and clinical PD-1 blockade in B-cell lymphomas. *Blood*. 2018;131(1):68-83.
 55. Sallusto F, Geginat J, Lanzavecchia A. Central memory and effector memory T cell subsets: function, generation, and maintenance. *Annu Rev Immunol*. 2004;22(1):745-763.
 56. Ansell SM, Minnema MC, Johnson P, et al. Nivolumab for relapsed/refractory diffuse large B-cell lymphoma in patients ineligible for or having failed autologous transplantation: a single-arm, phase II study. *J Clin Oncol*. 2019;37(6):481-489.
 57. Walker MP, Stopford CM, Cederlund M, et al. FOXP1 potentiates Wnt/β-catenin signaling in diffuse large B cell lymphoma. *Sci Signal*. 2015;8(362):ra12.
 58. Flori M, Schmid CA, Sumrall ET, et al. The hematopoietic oncprotein FOXP1 promotes tumor cell survival in diffuse large B-cell lymphoma by repressing S1PR2 signaling. *Blood*. 2016;127(11):1438-1448.
 59. Meyer PN, Fu K, Greiner TC, et al. Immunohistochemical methods for predicting cell of origin and survival in patients with diffuse large B-cell lymphoma treated with rituximab. *J Clin Oncol*. 2011;29(2):200-207.
 60. Gascogne DM, Banham AH. The significance of FOXP1 in diffuse large B-cell lymphoma. *Leuk Lymphoma*. 2017;58(5):1037-1051.
 61. van Keimpema M, Grüneberg LJ, Schilder-Tol EJ, et al. The small FOXP1 isoform predominantly expressed in activated B cell-like diffuse large B-cell lymphoma and full-length FOXP1 exert similar oncogenic and transcriptional activity in human B cells. *Haematologica*. 2017;102(3):573-583.
 62. Huong T, Kobayashi M, Nakata M, et al. In vivo analysis of Aicda gene regulation: a critical balance between upstream enhancers and intronic silencers governs appropriate expression. *PLoS One*. 2013;8(4):e61433.
 63. Crouch EE, Li Z, Takizawa M, et al. Regulation of AID expression in the immune response. *J Exp Med*. 2007;204(5):1145-1156.
 64. Sciammas R, Shaffer AL, Schatz JH, Zhao H, Staudt LM, Singh H. Graded expression of interferon regulatory factor-4 coordinates isotype switching with plasma cell differentiation. *Immunity*. 2006;25(2):225-236.
 65. Matsumoto Y, Marusawa H, Kinoshita K, et al. Helicobacter pylori infection triggers aberrant expression of activation-induced cytidine deaminase in gastric epithelium. *Nat Med*. 2007;13(4):470-476.
 66. Dedeoglu F, Horwitz B, Chaudhuri J, Alt FW, Geha RS. Induction of activation-induced cytidine deaminase gene expression by IL-4 and CD40 ligation is dependent on STAT6 and NFκB. *Int Immunol*. 2004;16(3):395-404.
 67. Pasqualucci L, Bhagat G, Jankovic M, et al. AID is required for germinal center-derived lymphomagenesis. *Nat Genet*. 2008;40(1):108-112.
 68. Hasham MG, Donghia NM, Coffey E, et al. Widespread genomic breaks generated by activation-induced cytidine deaminase are prevented by homologous recombination. *Nat Immunol*. 2010;11(9):820-826.

69. Liu M, Duke JL, Richter DJ, et al. Two levels of protection for the B cell genome during somatic hypermutation. *Nature*. 2008; 451(7180):841-845.
70. Robbiani DF, Nussenzweig MC. Chromosome translocation, B cell lymphoma, and activation-induced cytidine deaminase. *Annu Rev Pathol*. 2013;8(1):79-103.
71. Pasqualucci L, Neumeister P, Goossens T, et al. Hypermutation of multiple proto-oncogenes in B-cell diffuse large-cell lymphomas. *Nature*. 2001;412(6844):341-346.
72. Pettersen HS, Galashevskaya A, Doseth B, et al. AID expression in B-cell lymphomas causes accumulation of genomic uracil and a distinct AID mutational signature. *DNA Repair (Amst)*. 2015;25:60-71.
73. Lossos IS, Levy R, Alizadeh AA. AID is expressed in germinal center B-cell-like and activated B-cell-like diffuse large-cell lymphomas and is not correlated with intraclonal heterogeneity. *Leukemia*. 2004;18(11): 1775-1779.
74. Robbiani DF, Bothmer A, Callen E, et al. AID is required for the chromosomal breaks in c-myc that lead to c-myc/IgH translocations. *Cell*. 2008;135(6):1028-1038.
75. Kovalchuk AL, duBois W, Mushinski E, et al. AID-deficient Bcl-xL transgenic mice develop delayed atypical plasma cell tumors with unusual Ig/Myc chromosomal rearrangements. *J Exp Med*. 2007;204(12):2989-3001.
76. Takizawa M, Tolarová H, Li Z, et al. AID expression levels determine the extent of cMyc oncogenic translocations and the incidence of B cell tumor development. *J Exp Med*. 2008; 205(9):1949-1957.
77. Ramiro AR, Jankovic M, Eisenreich T, et al. AID is required for c-myc/IgH chromosome translocations in vivo. *Cell*. 2004;118(4):431-438.
78. Kiyasu J, Miyoshi H, Hirata A, et al. Expression of programmed cell death ligand 1 is associated with poor overall survival in patients with diffuse large B-cell lymphoma. *Blood*. 2015; 126(19):2193-2201.
79. Goodman A, Patel SP, Kurzrock R. PD-1-PD-L1 immune-checkpoint blockade in B-cell lymphomas. *Nat Rev Clin Oncol*. 2017;14(4): 203-220.
80. Andorsky DJ, Yamada RE, Said J, Pinkus GS, Betting DJ, Timmerman JM. Programmed death ligand 1 is expressed by non-hodgkin lymphomas and inhibits the activity of tumor-associated T cells. *Clin Cancer Res*. 2011; 17(13):4232-4244.
81. Rossille D, Gressier M, Damotte D, et al; Groupe Ouest-Est des Leucémies et Autres Maladies du Sang. High level of soluble programmed cell death ligand 1 in blood impacts overall survival in aggressive diffuse large B-Cell lymphoma: results from a French multicenter clinical trial. *Leukemia*. 2014;28(12): 2367-2375.
82. Georgiou K, Chen L, Berglund M, et al. Genetic basis of PD-L1 overexpression in diffuse large B-cell lymphomas. *Blood*. 2016; 127(24):3026-3034.
83. Rimsza LM, Roberts RA, Miller TP, et al. Loss of MHC class II gene and protein expression in diffuse large B-cell lymphoma is related to decreased tumor immunosurveillance and poor patient survival regardless of other prognostic factors: a follow-up study from the Leukemia and Lymphoma Molecular Profiling Project. *Blood*. 2004;103(11):4251-4258.
84. Brown PJ, Wong KK, Felce SL, et al. FOXP1 suppresses immune response signatures and MHC class II expression in activated B-cell-like diffuse large B-cell lymphomas. *Leukemia*. 2016;30(3):605-616.
85. Gowrishankar K, Gunatilake D, Gallagher SJ, Tiffen J, Rizos H, Hersey P. Inducible but not constitutive expression of PD-L1 in human melanoma cells is dependent on activation of NF- κ B. *PLoS One*. 2015;10(4):e0123410.
86. Huang G, Wen Q, Zhao Y, Gao Q, Bai Y. NF- κ B plays a key role in inducing CD274 expression in human monocytes after lipo-polysaccharide treatment. *PLoS One*. 2013; 8(4):e61602.
87. Peng J, Hamanishi J, Matsumura N, et al. Chemotherapy Induces Programmed Cell Death-Ligand 1 Overexpression via the Nuclear Factor- κ B to Foster an Immunosuppressive Tumor Microenvironment in Ovarian Cancer. *Cancer Res*. 2015;75(23): 5034-5045.
88. Lim SO, Li CW, Xia W, et al. Deubiquitination and Stabilization of PD-L1 by CSN5. *Cancer Cell*. 2016;30(6):925-939.
89. Heyman B, Yang Y. New developments in immunotherapy for lymphoma. *Cancer Biol Med*. 2018;15(3):189-209.
90. Merryman RW, Armand P, Wright KT, Rodig SJ. Checkpoint blockade in Hodgkin and non-Hodgkin lymphoma. *Blood Adv*. 2017;1(26): 2643-2654.
91. Nastoupil L, Westin JR, Fowler NH, et al. High complete response rates with pembrolizumab in combination with rituximab in patients with relapsed follicular lymphoma: results of an open-label, phase II study [abstract]. *Blood*. 2017;130(suppl 1). Abstract 414.
92. Palmer AC, Sorger PK. Combination cancer therapy can confer benefit via patient-to-patient variability without drug additivity or synergy. *Cell*. 2017;171(7): 1678-1691.

MGI Lit Triage Supplemental Data



blood[®]

2019 133: 2401-2412
doi:10.1182/blood.2018889931 originally published online
April 11, 2019

PD-1/PD-L1 immune checkpoint and p53 loss facilitate tumor progression in activated B-cell diffuse large B-cell lymphomas

Marién Pascual, María Mena-Varas, Eloy Francisco Robles, Maria-Jose Garcia-Barchino, Carlos Panizo, Sandra Hervas-Stubbs, Diego Alignani, Ainara Sagardoy, Jose Ignacio Martínez-Ferrandis, Karen L. Bunting, Stephen Meier, Xavier Sagaert, Davide Bagnara, Elizabeth Guruceaga, Oscar Blanco, Jon Celay, Alvaro Martínez-Baztan, Noelia Casares, Juan José Lasarte, Thomas MacCarthy, Ari Melnick, Jose Angel Martínez-Climent and Sergio Roa

Updated information and services can be found at:
<http://www.bloodjournal.org/content/133/22/2401.full.html>

Articles on similar topics can be found in the following Blood collections
[Immunobiology and Immunotherapy](#) (5692 articles)
[Lymphoid Neoplasia](#) (3075 articles)

Information about reproducing this article in parts or in its entirety may be found online at:
http://www.bloodjournal.org/site/misc/rights.xhtml#repub_requests

Information about ordering reprints may be found online at:
<http://www.bloodjournal.org/site/misc/rights.xhtml#reprints>

Information about subscriptions and ASH membership may be found online at:
<http://www.bloodjournal.org/site/subscriptions/index.xhtml>

SUPPLEMENTARY METHODS

Genetically modified mice

Single mouse strains were obtained from The Jackson Laboratory, including *p53^F* (B6.129P2-*Trp53^{tm1Brn}*/J; stock 008462; abbreviated p), *Blimp1^F* (B6.129-*Prdm1^{tm1Clme}*/J; stock 008100; abbreviated B), *IKK2caGFP^{stopF}* (B6(Cg)-*Gt(ROSA)26Sor^{tm1(Ikkbb)Rsky}*/J; stock 008242; abbreviated I), *Cy1-cre* (B6.129P2(Cg)-*Ighg1^{tm1(IRES-cre)Cgn}*/J; stock 010611; abbreviated C), and *eYFP^{stopF}* (B6.129X1-*Gt(ROSA)26Sor^{tm1(EYFP)Cos}*/J; stock 006148; abbreviated Y). Mice were successively crossed to generate the following compound strains: YC, BIC, pBIC (Fig. 1a), where all conditional alleles were maintained as homozygous except for the YFP reporter and Cg1-cre alleles that were used as heterozygous. Multi-lesion compound mice were housed in a specific pathogen-free animal facility. Eight- to 10-week-old mice were chronically immunized i.p. with 10⁹ SRBCs every 20 days until signs of tumor development occurred and required euthanasia. All animal care and procedures were approved by the Ethical Committee of Animal Experimentation of the *Center for Applied Medical Research* (CIMA) and the ISPLN Health Department.

Human samples and data

Normal fresh human tonsils (n=4) and FFPE blocks from a retrospective collection of DLBCL lymphoma patients (n=112) were studied with the approval of the Clinical Research Ethics Committee of the Clinica Universidad de Navarra and in accordance with ethical guidelines at the University Hospital of Katholieke Universiteit Leuven. In addition, we used six publicly available datasets from the NCBI GEO repository, which include gene expression data from a total of 1,135 DLBCL patients (GSE32018, GSE25639, GSE34171, GSE10846, GSE31312) and 29 control primary samples of human naïve and GC cells (GSE49629, GSE32018, GSE25639). Associations of clinical and molecular data (e.g. overall survival, genetic mutations, gene expression and immunohistochemical information) were explored on publicly available metadata from 233 R-CHOP treated DLBCL cases (GSE10846) or from 1,001 newly diagnosed DLBCL patients from Reddy et al.³⁹.

Primary cells and cell lines

Fresh human tonsils and murine spleens were either fixed in 10% buffered formalin and embedded in paraffin or submitted to cellular disaggregation, followed by lysis of erythrocytes

using ACK buffer. Then, single-cell preparations were either frozen in 90% FCS and 10% DMSO or submitted to fresh cellular sorting. Magnetic-based cell sorting (AutoMACS) was used to isolate naïve (IgD^+) and GC ($\text{IgD}^- \text{CD71}^+$) cells from human tonsils for expression analysis, and murine B cells (CD19^+) for *ex vivo* activation during 72h in complete RPMI media supplemented with IL4 (50ng/ml) plus LPS (50 $\mu\text{g}/\text{ml}$). FACS AriaII sorter (BD, 3 laser) was used to sort different populations from murine spleens after exclusion of dead cells with 7AAD. These populations included reporter positive B cells ($\text{B220}^{+/\text{low}} \text{GFP}^+$) from murine tumors, as well as resting naïve B cells ($\text{B220}^+ \text{CD38}^+ \text{Fas}^-$), GC ($\text{B220}^+ \text{CD38}^{\text{low}} \text{Fas}^+$) and PCs ($\text{B220}^{\text{low}} \text{CD138}^+$) from control YC mice. Human DLBCL cell lines were grown in media containing 10% FBS, 2% penicillin/streptomycin and IMDM medium (for OCI-Ly1 and OCI-Ly7 cells) or RPMI medium (for OCI-Ly8, SC, RL and U2932 cells). Human OCI-Ly3 and OCI-Ly10 DLBCL cells were grown in IMDM media containing 20% of human serum, 50 μM β -mercaptoethanol and 2% penicillin/streptomycin. The murine B-cell lymphoblastic CH12F3-2 cell line was maintained in RPMI supplemented with 10% FBS, 5% NCTC-109, 50 μM β -mercaptoethanol and 5% penicillin/streptomycin, and was activated *in vitro* with the CIT cocktail containing functional grade purified anti-mCD40 (2 $\mu\text{g}/\text{ml}$, Thermofisher, 1C10), recombinant mouse IL-4 (10 ng/ml) and recombinant human TGF- β (1ng/ml).

Immunohistochemistry

Haematoxylin and eosin and antibody staining were performed on murine spleens, human tonsils or human lymphoma biopsies using standard procedures and our previous experience³⁷. The antibodies used were against p53 (Novocastra p53-CM5P-L, 1:500), B220 (Santa Cruz sc19597, 1:50), ki67 (Thermo Scientific RM9106, 1:100), m/hFOXP1 (Abcam ab16645, 1:1000), mAID (Millipore MABF63, 1:50), hAID (Cell Signaling 4959, 1:100), GFP (Abcam ab6556, 1:1000), CD4 (Abcam ab183685, 1:1000), and CD8 (Cell Signaling 98941, 1:400). Staining for p53 was also performed in the murine spleen of one YC reporter mouse that had been exposed to 5 Gy total body γ -irradiation as positive control for p53 activation. When indicated, chromogenic double staining using DAB and Permanent Red was used to detect AID and FOXP1, respectively, in normal primary tissues. Slides were viewed with a light microscope and digitized using an Aperio Scanscope whole-slide scanner at 20X magnification. Murine and human images were reviewed by expert pathologists (OB and XS, respectively). DLBCL patients in the CHOP-like treatment cohort were classified as GCB or non-GCB by a pathologist (XS) using the Hans Algorithm, and were scored for FOXP1/AID

immunostaining as either negative (score 0), weakly positive (score +1), moderately positive (score +2) or strongly positive (score 3+). We then modeled the distribution of FOXP1/AID scores and used the estimated median to stratify patients as either negative or positive for the corresponding IHC staining (Fig. S3).

Quantitative real time PCR (qRT-PCR)

Total RNA was extracted from sorted cells using TRIzol (Invitrogen) as described in manufacturer's protocol. RNA was converted into cDNA using random hexanucleotides and Perfect Real Time kit (Takara). Quantitative RT-PCR was performed with SYBR green (Applied Biosystems) in a ViiA7 real-time thermal cycler (Applied Biosystems). cDNAs were tested in triplicate and data were calculated and normalized to the *GAPDH* housekeeping gene.

RNA sequencing and analysis

RNA isolated from FACS-sorted reporter positive splenic B cells ($B220^+GFP^+/YFP^+$) from a total of 12 mice (6 pBIC, 3 BIC and 3 YC as controls) was subjected to quality control by Agilent Bioanalyzer, followed by general transcriptome library preparation and massive sequencing performed by BGI Tech (BGI, Shenzhen, China) using the Illumina HiSeq4000 platform with the paired-end 100-bp read option. After quality control analysis using FastQC, checked reads were aligned to mouse mm10 genome using STAR. Then, Gencode M13 was used to generate gene annotations and gene expression quantification was computed using read counts of exonic gene regions with featureCounts, followed by normalization with edgeR and voom. After quality assessment and outlier detection with R/Bioconductor, genes with read counts lower than 6 in more than the 50% of the samples of all the studied conditions (BIC, pBIC and YC) were considered as not expressed in the experiment under study. LIMMA (Linear Models for Microarray Data) was used to identify the genes with significant differential expression between experimental conditions, using $FC > 1.5$ and $B > 0$ as cut off. Scatter plots, hierarchical clustering and heatmaps of \log_2 fold-changes in expression were generated in R/Bioconductor. The Chimera package applied to the chimeric output of the STAR aligner was used to detect gene fusion events in the RNAseq data. Gene ontology analysis of differentially expressed genes was performed through PANTHER classification system (<http://www.pantherdb.org/>). Expression levels by RNAseq of 18 murine orthologue genes previously associated in human with ABC/GCB subtypes³⁹ were used to classify murine lymphomas according to their combined RNAseq subtype score. Briefly, this subtype score

was computed as in the human setting³⁹ by subtracting in each sample the average of the z-scores for the GCB-related genes (GCB score) to the average of the z-scores for the ABC-related genes (ABC score). A sample was classified as ABC-DLBCL if the RNAseq subtype score was > 0.25 and its GCB score was < 0.75. Alternatively, a sample was classified as GCB-DLBCL if the RNAseq subtype score was < -0.25 and its ABC score < 0.75. As validation for our approach, we were able to confirm the expected classification of normal GC B cells - FACS-sorted from YC control spleens - as GCB-like cells ([Fig. 1d](#)).

Chromatin immunoprecipitation

Human DLBCL cells (OCI-Ly1) and resting or cytokine-activated murine cells (CH12 and splenic CD19⁺) were cross-linked with 1% formaldehyde and quenched with 0.125M glycine, followed by nuclei isolation and lysis in RIPA buffer. After sonication, immunoprecipitations were performed using 10µg Rabbit polyclonal antibody against FOXP1 (Abcam ab16645) or rabbit IgG antibody as isotype control (Abcam ab46540). DNA fragments enriched by ChIP and input fractions were either submitted to qRT-PCR analysis or constructed into deep-sequencing libraries following Illumina protocol and sequenced on a HiSeq2000 (Illumina) platform. Sequenced DNA tags were aligned against the reference human genome hg19 and peaks were called using the Chipseeqr algorithm (Elemento lab at Weill Cornell Medical College) with stringent statistical criteria (*P*-value cutoff of 10⁻¹⁵) and compared to the input control. FOXP1 occupancy was enriched near gene transcription start sites (TSSs) and Biomart analysis (Bioconductor) located these peaks at -2kb to +5kb from TSS of 11,693 genes ([Supplementary Table 5](#)), from which a significant fraction exhibited FOXP1 occupancy downstream of the TSS, as in the *AID* gene ([Fig. 2e](#)). To further confirm the specificity of the FOXP1 binding, we used the MEME-chip algorithm for identification of RTAAAYA as an enriched motif within FOXP1 peaks (*E*-value = 2.7e⁻¹¹²), and the TOMTOM algorithm to verify that it consistently matched the canonical GTAAACCA motif described for FOXP1 in the JASPAR DNA motif database (*P*-value = 0.00019) and in B cells¹⁷. Association of FOXP1 peaks with chromatin states was performed using the ENCODE chromHMM data from the B lymphoid GM12878 cell line mapped to hg19 (11 state segmentations) or the B lymphoblastoid CH12 cell line mapped to mm9 (7 state segmentation). Wiggle tracks were visualized using the UCSC Genome Browser. Additional processed ChIP-seq data in BED format showing FOXP1 occupancy in other human ABC- (OCI-Ly10, OCI-Ly3) and GCB-like (OCI-Ly7) DLBCL cell lines was available from van Keimpema et al.¹⁹.

RNA interference

Four different sequences targeting the 3'UTR region of *hFOXP1* were designed (ThermoFisher), from which only 2 (siFOXP1#1: 5'-CAACTTAGCCAGCGCAATA-3' and siFOXP1#2: 5'-GCCAAGGCCTTCTGACAATT-3') were able to effectively knock-down *FOXP1* expression in human cell lines compared to scramble siRNA. In the murine cell line CH12, validated siGENOME SMARTpool siRNAs (Dharmacon) targeting mFOXP1 (M-065400-00-0005) or non-targeting control (D-001206-13-05) were used. All siRNAs were transiently transfected into cells by nucleofection with Amaxa (Lonza) and harvested 48h later for RNA extraction and transcriptional analysis by qRT-PCR or expression microarray. Data collected from three replicates of each siRNA was averaged and normalized to the siRNA control group, and therefore differences were represented as fold-changes relative to the scramble control.

Microarray expression analysis

Triplicate RNA samples from OCI-ly1 cells after FOXP1 silencing by two different siRNAs (N=3+3) and one scramble control (N=3) were submitted to quality control by Agilent Bioanalyzer prior to hybridization to the NimbleGen Human_60mer_1in2 platform (GPL15088). R and Bioconductor were used to perform RMA-normalization, log2 transformation, average between biological replicates, subtraction of averages from the negative control and comparative t-test analysis. A comprehensive set of gene expression profiles directly affected by FOXP1 silencing was obtained by overlapping with the ChIP-seq list of FOXP1 bound genes.

VDJ-IgH seq

Full-length VDJ-IgH sequencing of FACS-sorted naïve (N=4), GC (N=4) and tumoral BIC (N=2) or pBIC (N=2) B cells was performed as previously described in the human setting³⁸ but with new primers specifically designed for the murine IgH repertoire ([Supplementary Table 6](#)). Briefly, total RNA was extracted from the cell sorted population and the equivalent amount of RNA from 10,000 cells was further purified using magnetic beads to isolate mRNA. During cDNA synthesis, a 16mer unique molecular identifier together with a partial Illumina adapter was added and used later to perform a two-step semi-nested PCR amplification with universal Illumina adapters and a mix of CH isotype-specific reverse primers. Amplified V-D-J-C_{5'} IgH

sequences were submitted to massive sequencing using the Illumina MiSeq platform (v3 2x300 kit, Illumina MS-102-3003). Preprocessing, including assembly of raw paired-end reads and error-correction, was performed using the SHMPrep program (<http://www.ams.sunysb.edu/~maccarth/software.html>). IMGT/HighV-QUEST was used to identify V(D)J and CDR3 segments, followed by the DefineClones script (in the Change-O package) to build clonally related groups of sequences based on CDR3 similarity that were most likely descended from the same B cell. Custom Matlab scripts (available upon request) were next used to analyze the clonal groups for BCR diversity by (i) calculating frequencies of unique mutations compared to germline VDJ-IgH references (SHM), (ii) computing the number of unique sequences or members that were assigned to the same CDR3 clonal group (intraclonal lineage diversity), (iii) defining clone size as the number of distinct barcoded single molecules identified, and (iv) recognizing the isotype-specific reverse primer that predominates across clonal sequences (CSR).

Flow cytometry

Cells were incubated with the respective antibodies diluted in FACS buffer for 20 min at 4 °C for surface antigen staining or were fixed and permeabilized using the Mouse Regulatory T cell Staining Kit (Invitrogen) for intracellular staining of TRegs. Non-specific binding of Fc receptor was blocked using a FcBlock. The following marker combinations were used to define T cells (CD3⁺ CD4⁺/CD8⁺), NKT cells (CD3⁺ NKX1.1⁺), NK cells (CD3⁻ NKX1.1⁺), TRegs (CD4⁺ CD25⁺ FOXP3⁺), macrophages (CD11b⁺ F4/80⁺ Ly6G⁻ Ly6C⁻), dendritic cells (CD11b⁺ F4/80⁻ CD11c⁺ IA^{b+}), GrMDC (CD11b⁺ F4/80⁻ noDCs Ly6G⁺ Ly6C⁻), and MoMDC (CD11b⁺ F4/80⁻ noDCs Ly6G⁻ Ly6C⁺). Normal (GFP⁻ or YFP⁺ when obtained from control YC mice) and malignant B cells (GFP⁺, which served as a reporter gene to detect CRE-mediated recombination of mutant alleles) were stained for surface markers B220, CD19, CD20 and PD-L1. T cell exhaustion was explored by staining of PD1, LAG3 and 2B4, while activation was explored by staining of CD44 and CD62L. We discarded the possibility of an artefactual competition between the anti-PD-1 mAbs used for treatment (clone RMP1-14, BioXcell) and for flow cytometry (clone 29F.1A12, Biolegend), as we were able to clearly detect PD-1⁺ cells by FACS regardless they were previously pre-treated or not for 1 h on ice with anti-PD-1-RMP1-14 (Fig. S6). Cell death in YFP^{+/GFP⁺ reporter cells was studied using Annexin V-APC/7AAD staining (Thermo Fisher A35110) according to manufacturer's recommendations. For flow cytometric analysis of γH2AX intracellular accumulation in}

YFP⁺/GFP⁺ reporter cells, cells were fixed and permeabilized using BD Perm/wash and Cytofix/Cytoperm buffers, followed by staining with anti- γ H2AX-BV421 (BD 564720). Surface IgM or IgG expression was also measured in YFP⁺/GFP⁺ reporter cells. Data were acquired on FACSCantoII flow cytometer (BD) and analyzed using FlowJo software (TreeStar). Cytometry and sorting settings for the use of the following antibodies were initially validated in single-staining positive and negative controls: B220-APC/BV421 (Biolegend, RA3-6B2), CD38-PE.cy7 (Biolegend, 90), Fas-PE (BD Biosciences, Jo2), CD138-PE (BD Biosciences, 281-2), CD3-APC (Biolegend, 145-2C11), CD4-BV510 (Biolegend, RM4-5), CD8-PerCP.cy5.5 (Biolegend, CD8 α 53-6.7), CD19-PE.cy7 (Biolegend, 6D5), CD20-APC (Biolegend, SA275A11), NKX1.1-PE (Biolegend, PK136), CD25-APC (Biolegend, PC61), FOXP3-PE (BD Biosciences, R16-715), CD11b-BV510 (Biolegend, M1/70), CD11c-PE (Biolegend, N418), F4/80-APC (Biolegend, BM8), Ly6G-BV421 (BD Biosciences, 1A8), Ly6C-PerCP.cy5.5 (Biolegend, HK1.4), IAb-PE.cy7 (Biolegend, AF6-120.1), PD-L1-PE (Thermofisher, MIH5), PD-1 (Biolegend, 29F.1A12), LAG3-PE (Biolegend, C9B7W), 2B4-PerCP.cy5.5 (Biolegend, B6-458.1), CD44-PE (Biolegend, IM7), CD62L-PE.cy7 (Biolegend, MEL-14), γ H2AX-BV421 (BD Biosciences, N1-431), IgG-BV510 (Biolegend, Poly4053), IgM-APC (BD Biosciences, II/41).

t-SNE analysis

Raw flow cytometry files from basal YC (N=4), BIC (N=4) and pBIC (N=4) or from mice treated for 4 weeks with α PD-1 (N=3), α CD20 (N=3), or α CD20+ α PD-1 (N=3) were first pre-processed in FlowJo, where doublets were excluded using FSC-H/FSC-A and lymphocytes were identified using FSC-A/SSC-A. Then, cells of interest (i.e. CD4⁺, CD8⁺ and GFP⁺ cells) were gated, exported as single FCS files and concatenated again for each sample to further exclude unstained cells. These processed FCS files were further loaded into the R package Cytofkit for random downsampling of 5,000 cells from each sample without replacement and dimensionality reduction analysis using Rphenograph clustering method and t-SNE visualization. Unsupervised phenograph clusters were further grouped and annotated according to hierarchical clustering of key expression markers (i.e. CD8, CD4, GFP, PD-1, LAG3, 2B4 in the exhaustion panel and CD8, CD4, CD44, CD62L in the activation panel) explored through heatmap analysis.

Murine *in vivo* treatments

Mice were randomly allocated in the experimental groups and treated intraperitoneally once a week with either anti-mouse anti-CD20 (clone 5D2, isotype IgG2a, Genentech), anti-mouse anti-PD1 (clone RMP1-14, isotype IgG2a, BioXcell), a combination of both or saline vehicle. Doses of 200ug/mouse of each antibody were injected intraperitoneally in a final volume of 200 µL of phosphate buffered saline. All treatments started when pBIC mice were between 180 and 200 days old. This time was considered the beginning of the lymphoma progression phase since animals already evidence incipient splenomegaly, which can be confirmed by either echography or palpation, and survival rates start to decline (Fig. S7). Treatment regimens included three modalities: (i) full-regimen, where mice were treated for 8 consecutive weeks and then left for study of overall survival, (ii) half-regimen, where mice were sacrificed after 4 cycles of treatment and then submitted to immunohistochemistry, cytometry and t-SNE analysis, or (iii) relapse study, where mice were treated for 4 weeks and then rested without any treatment for additional 4 or 8 weeks before analysis of the reappearance of normal or GFP⁺ malignant cells by cytometry. Depletion studies were performed by intraperitoneal injection of anti-CD8β (clone 53-5.8, isotype IgG1, BioXcell) or anti-CD4 (clone GK1.5, isotype IgG2b, BioXcell) mAbs, starting simultaneously to the anti-CD20/anti-PD-1 combination and maintaining a weekly administration of 100 µg/mouse, beyond the end of the combination treatment, until death or appearance of signs of tumor development or disease that required euthanasia.

Echography imaging

Mice spleens were imaged by ultrasound once a week at four consecutive times in treated and control animals (a minimum of 3 animals per group), using a Vevo 770® High-Resolution Imaging System (VisualSonics). Briefly, fur was removed from the abdomen of mice using an electric razor and depilatory cream, followed by a thorough wash of the skin with water. Mice were maintained anesthetized by inhalation of isoflurane for the duration of the imaging and a heat lamp was kept over the mice at all times to preserve body temperature. Sonographer was blinded to any treatment data and splenomegaly was evaluated by determination of the spleen transversal area (mm²). Consecutive measurements at different times during treatment were normalized for each mouse to the first measurement obtained during the initial echography at the beginning of the treatment.

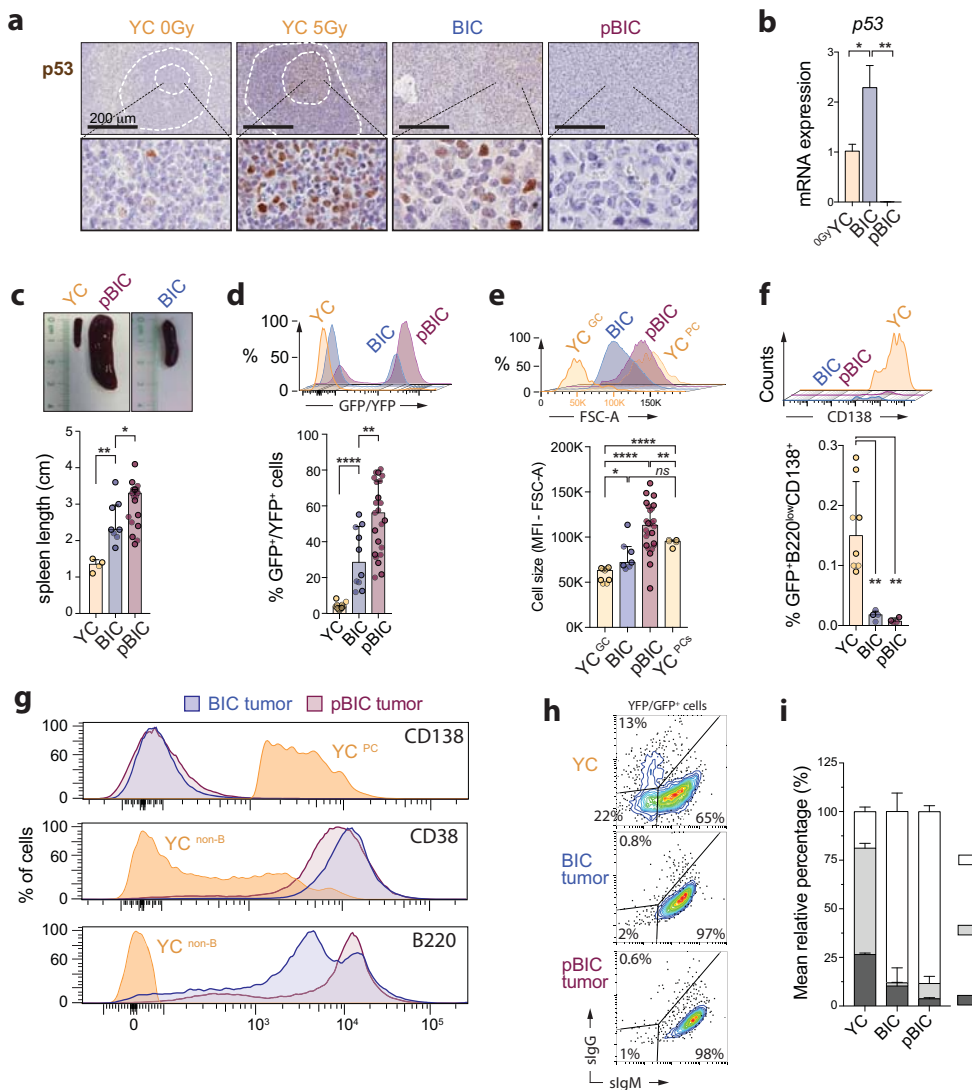
Statistical Analysis

All statistical analysis was performed using GraphPad Prism version 7.0. Data have been plotted as mean \pm standard error of the mean (SEM) for samples following a normal (Gaussian) distribution, for which *P*-values were calculated by unpaired Student's *t* tests. Alternatively, Mann-Whitney tests were used and data was plotted as median \pm interquartile range. Correlations in gene expression changes were calculated using Pearson's analysis. Covariation of IHC scores was analyzed by Spearman nonparametric correlation. Survival *P*-values were calculated by log-rank Mantel-Cox or Gehan-Breslow-Wilcoxon tests with extra weight for early time points. DLBCL subtype distributions of patients further stratified according to IHC (BCL2, cMYC, DEL, p53 mutations) or gene expression criteria (FOXP1/AID) were analyzed by Chi-square tests. Statistical significance is indicated as follows: **P* < 0.05, ***P* < 0.01, ****P* < 0.001 and *****P* < 0.0001.

Data availability

The data discussed in this publication have been deposited in NCBI's Gene Expression Omnibus (GEO) and are accessible through GEO SuperSeries accession number GSE116290.

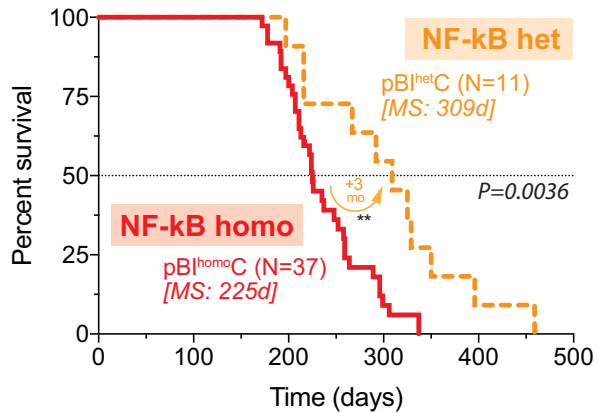
Supplementary Figure S1



Supplementary Figure S1. Supplemental data supporting that conditional deletion of p53 cooperates with constitutive canonical NF-κB and *Blimp1* loss in ABC-DLBCL lymphomagenesis.

(a) Representative immunohistochemical staining of p53 in normal or irradiated murine splenic GCs and lymphomas. Scale bar, 200 μm; magnification, x40. **(b)** Expression analysis of *Trp53* by qRT-PCR of FACS-sorted reporter-positive normal and lymphoma splenic B cells from non-irradiated mice (n=3 animals). **(c)** Representative photos and comparative lengths of spleens from YC control and moribund BIC/pBIC mice. **(d)** Representative FACS profiles and comparative percentages of normal YFP⁺ GC cells from spleens of YC controls or expanding GFP⁺ malignant cells from moribund BIC/pBIC mice **(e)** Representative FACS profiles and cellular sizes of reporter-positive cells from YC control mice, corresponding to normal GC B cells or plasma cells (PCs), and from murine B-cell lymphomas. **(f)** Representative FACS profiles and comparative percentages of reporter-positive splenic PCs (GFP⁺B220^{low}CD138⁺ cells) indicating terminal differentiation. **(g)** Representative FACS histograms for the levels of B cell-related surface markers in BIC/pBIC GFP⁺ murine lymphomas or in YC control plasma cells (PC) and non-B cells (YFP⁻B220⁻). **(h)** Representative FACS profiles for surface IgG or IgM expression in normal YFP⁺ GC cells from YC controls or GFP⁺ BIC/pBIC tumors. **(i)** Comparative percentages of unique VDJ-IgH sequences showing the IgM, IgG or IgA isotype within reporter-positive murine control (n=4 YC) or lymphoma cells (n=2 BIC and 2 pBIC), as measured in the VDJ-IgH seq approach (see also Fig. 1i).

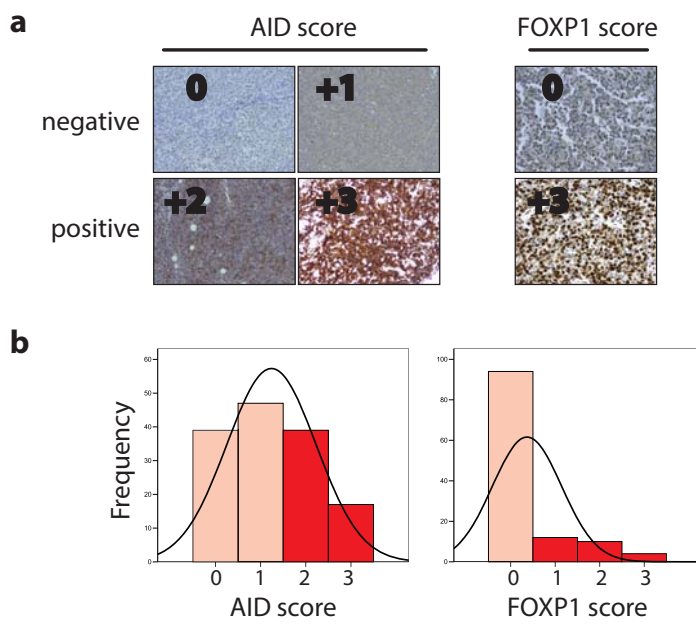
Supplementary Figure S2



Supplementary Figure S2. Supplemental data supporting that the levels and ongoing activity of NF- κ B signaling play an important additional role to p53 deficiency.

Overall survival of pBIC mice that carry only one copy of the ROSA26-stopF-IKK2ca-IRES-GFP allele (NF- κ B het) but are still homozygously deficient for p53 and Blimp1 (pBI het C), compared to the standard pBIC mice used throughout this work (NF- κ B homo), which are homozygous for the mutant IKK2ca allele (pBI homo C). Survival P -value was calculated by log-rank Mantel-Cox test.

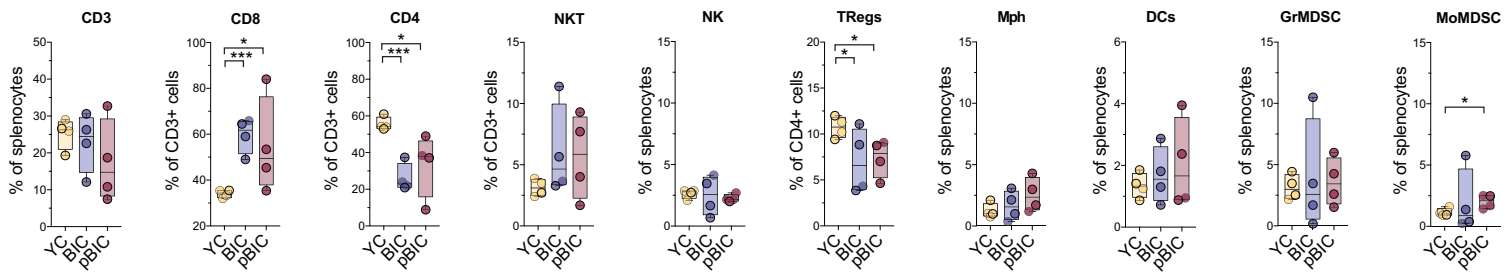
Supplementary Figure S3



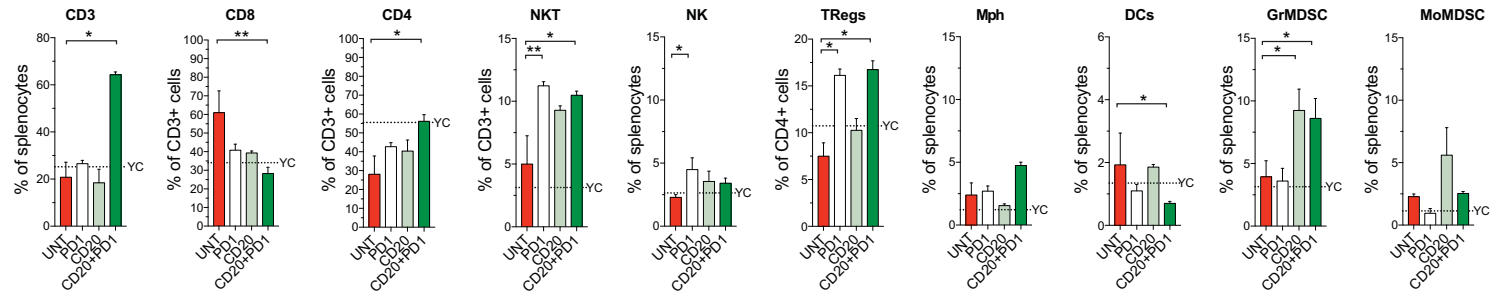
Supplementary Figure S3. Semi-quantitative score (**a**) and median distribution (**b**) of FOXP1 and AID protein expression by immunohistochemistry in a retrospective collection of 112 CHOP-like treated patients.

Supplementary Figure S4

a. Relative percentages of immune cells in basal control and murine ABC-DLBCLs

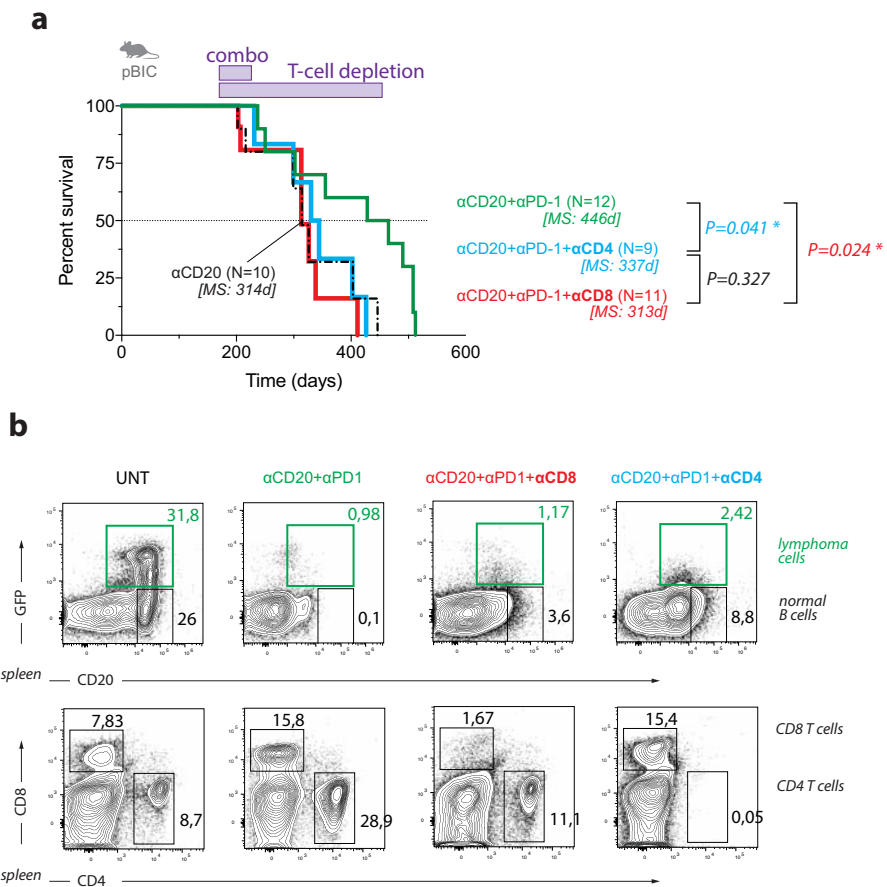


b. Relative percentages of immune cells in murine ABC-DLBCLs after 4 weeks of immunotherapy.



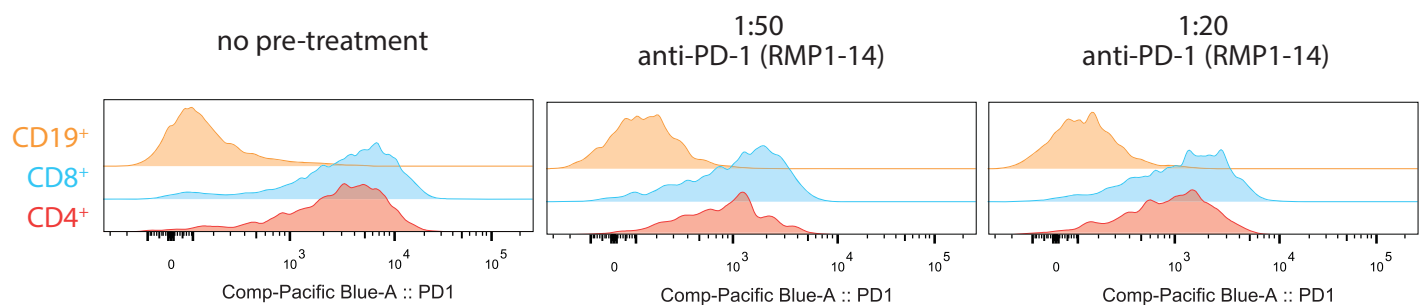
Supplementary Figure S4. Supplemental data obtained by FACS analysis, comparing the percentages of different immune cell populations in the spleen of **(a)** control YC mice, moribund BIC or pBIC mice with splenomegaly and evidence of lymphoma, and **(b)** pBIC mice treated with different immunotherapy combinations for 4 weeks.

Supplementary Figure S5



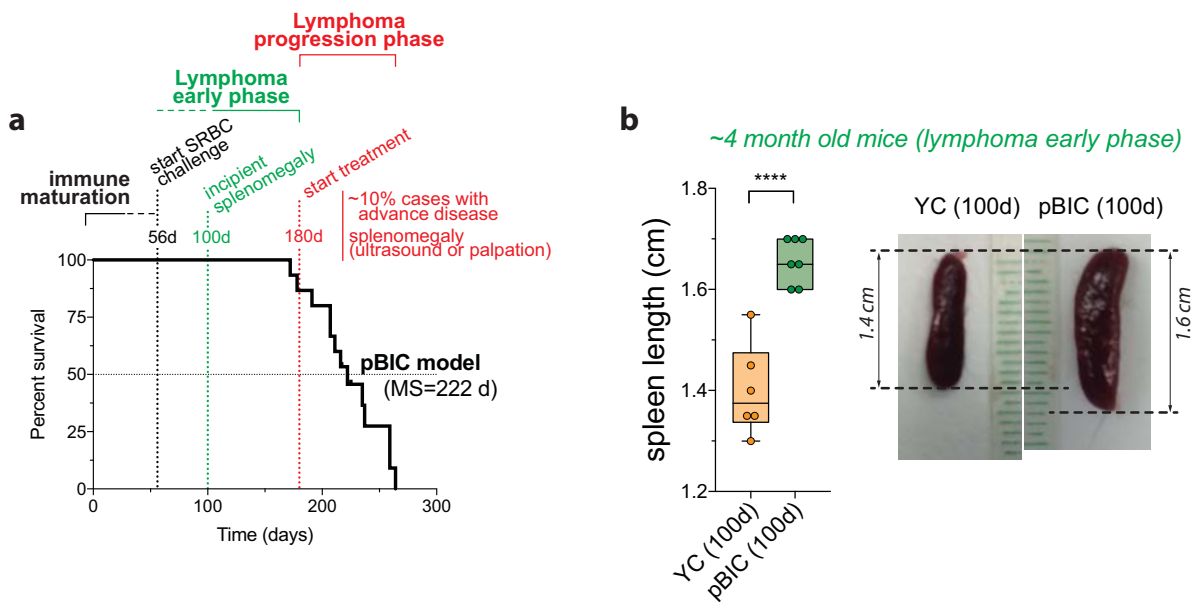
Supplementary Figure S5. Supplemental data supporting T cell-related immune-regulatory mechanisms in the anti-CD20/anti-PD-1 combination. **(a)** Overall survival of murine ABC-DLBCL pBIC mice treated with the anti-CD20/anti-PD-1 combination plus anti-CD8 or anti-CD4 T-cell depleting mAbs. UNT, untreated; MS, median survival. Survival *P*-values were calculated by log-rank Mantel-Cox tests. As indicated in Supplementary Methods and depicted in the bars above survival curves, combo treatments were administered i.p. weekly for 8 cycles (full-regimen), while anti-CD4/CD8 depleting mAbs were administered i.p. weekly until survival endpoint. **(b)** Representative FACS profiles of pBIC splenocytes from pBIC mice after 4 weeks receiving the indicated treatment (half-regimen modality, 4 cycles). A robust depletion of CD20⁺ cells, both GFP-reporter tumor cells and normal B cells, was confirmed in all immunotherapy treatments. Specific depletion of either CD8 or CD4 T cells was confirmed in the corresponding treatment groups.

Supplementary Figure S6



Supplementary Figure S6. Supplemental data obtained by FACS analysis, comparing PD-1 surface levels in splenic CD19⁺ B cells and CD4⁺ or CD8⁺ T cells from a pBIC murine lymphoma. Primary cells were pre-treated with different dilutions of anti-PD-1 (mAb clone RMP1-14 used for *in vivo* treatments) to demonstrate positive detection of PD-1 by FACS using mAb clone 29F.1A12 and, therefore, lack of epitope competition between these two mAbs.

Supplementary Figure S7



Supplementary Figure S7. Proposed scheme for lymphoma onset in the pBIC mice. **(a)** Treatments were initiated when pBIC mice were approximately 6 months old. At this time, 10% of animals had already died from lymphoma, splenomegaly was evident by either echography or palpation, and within the following 2 months survival curves would predict an aggressive progression of the disease for the remaining 90% of cases. **(b)** Minor, but incipient splenomegaly could already be detected in 4 month old mice. Additional details regarding murine *in vivo* treatments can be found in Supplementary Methods.